



HAL
open science

The CSES Global Geomagnetic Field Model (CGGM): An IGRF type global geomagnetic field model based on data from the China Seismo-Electromagnetic Satellite.

Yanyan Yang, Gauthier Hulot, Pierre Vigneron, Xuhui Shen, Zhima Zeren,
Bin Zhou, Werner Magnes, Nils Olsen, Lars Tøffner-Clausen, Jianpin Huang,
et al.

► To cite this version:

Yanyan Yang, Gauthier Hulot, Pierre Vigneron, Xuhui Shen, Zhima Zeren, et al.. The CSES Global Geomagnetic Field Model (CGGM): An IGRF type global geomagnetic field model based on data from the China Seismo-Electromagnetic Satellite.. Earth Planets and Space, In press. hal-03092984v1

HAL Id: hal-03092984

<https://hal.science/hal-03092984v1>

Submitted on 3 Jan 2021 (v1), last revised 12 Feb 2021 (v2)

HAL is a multi-disciplinary open access archive for the deposit and dissemination of scientific research documents, whether they are published or not. The documents may come from teaching and research institutions in France or abroad, or from public or private research centers.

L'archive ouverte pluridisciplinaire **HAL**, est destinée au dépôt et à la diffusion de documents scientifiques de niveau recherche, publiés ou non, émanant des établissements d'enseignement et de recherche français ou étrangers, des laboratoires publics ou privés.

1 **The CSES Global Geomagnetic Field Model (CGGM): An IGRF type global**
2 **geomagnetic field model based on data from the China Seismo-Electromagnetic**
3 **Satellite.**
4
5 **Yanyan Yang**, National Institute of Natural Hazards, Ministry of Emergency
6 Management of China, Beijing, 100085, China, youngyany@163.com
7 **Gauthier Hulot**, Université de Paris, Institut de physique du globe de Paris, CNRS,
8 F-75005 Paris, France, gh@ipgp.fr
9 **Pierre Vigneron**, Université de Paris, Institut de physique du globe de Paris, CNRS,
10 F-75005 Paris, France, vigneron@ipgp.fr
11 **Xuhui Shen**, National Institute of Natural Hazards, Ministry of Emergency
12 Management of China, Beijing, 100085, China, shenxh@seis.ac.cn
13 **Zhima Zeren**, National Institute of Natural Hazards, Ministry of Emergency
14 Management of China, Beijing, 100085, China, zerenzhima@qq.com
15 **Bin Zhou**, National Space Science Center, Chinese Academy of Sciences, Beijing,
16 100190, China, zhoubin@nssc.ac.cn
17 **Werner Magnes**, Space Research Institute, Austrian Academy of Sciences, Graz, 8042,
18 Austria, Werner.Magnes@oeaw.ac.at
19 **Nils Olsen**, DTU Space, National Space Institute, Technical University of Denmark,
20 2800 Kongens Lyngby, Denmark, nio@space.dtu.dk
21 **Lars Tøffner-Clausen**, DTU Space, National Space Institute, Technical University of
22 Denmark, 2800 Kongens Lyngby, Denmark, lastec@space.dtu.dk
23 **Jianpin Huang**, National Institute of Natural Hazards, Ministry of Emergency
24 Management of China, Beijing, 100085, China, xhhjp@126.com
25 **Xuemin Zhang**, Institute of Earthquake Forecasting, China Earthquake Administration,
26 Beijing, 100036, China, zhangxm96@126.com
27 **Shigeng Yuan**, DFH Satellite Co. Ltd., Beijing, 100081, China, sgyuan@sina.com
28 **Lanwei Wang**, Institute of Earthquake Forecasting, China Earthquake Administration,
29 Beijing, 100036, wanglw829@126.com

30 **Bingjun Cheng**, National Space Science Center, Chinese Academy of Sciences,
31 Beijing, 100190, China, chengbj@nssc.ac.cn
32 **Andreas Pollinger**, Space Research Institute, Austrian Academy of Sciences, Graz,
33 8042, Austria, andreas.pollinger@oeaw.ac.at
34 **Roland Lammegger**, Institute of Experimental Physics, Graz University of Technology,
35 Graz, 8010, Austria, roland.lammegger@tugraz.at
36 **Jianpin Dai**, Beijing Special Engineering Design and research Institute, Beijing,
37 100028, China, 13146635862@163.com
38 **Jun Lin**, China Centre for Resources Satellite Data and Application, Beijing, 100094,
39 China, 39889853@qq.com
40 **Feng Guo**, National Institute of Natural Hazards, Ministry of Emergency Management
41 of China, Beijing, 100085, China, Indlguofeng@163.com
42 **Jingbo Yu**, Hebei GEO University, Shijiazhuang 050031, China, jingboyu@126.com
43 **Jie Wang**, National Institute of Natural Hazards, Ministry of Emergency Management
44 of China, Beijing, 100085, China, 398080150@qq.com
45 **Yingyan Wu**, Institute of Earthquake Forecasting, China Earthquake Administration,
46 Beijing, 100036, China, wuyyan79@126.com
47 **Xudong Zhao**, Institute of Geophysics, China Earthquake Administration, Beijing,
48 100081, China, zxd9801@163.com
49 **Xinghong Zhu**, DFH Satellite Co. Ltd., Beijing, 100081, China, little_zhuxh@163.com
50 **Co-corresponding authors: Xuhui Shen**, shenxh@seis.ac.cn; **Gauthier Hulot**,
51 gh@ipgp.fr

52 **Abstract**

53 Using magnetic field data from the China Seismo-Electromagnetic Satellite (CSES)
54 mission, we derive a global geomagnetic field model, which we call the CSES Global
55 Geomagnetic Field Model (CGGM). This model describes the Earth's magnetic main
56 field and its linear temporal evolution over the time period between March 2018 and
57 September 2019. As the CSES mission was not originally designed for main field
58 modelling, we carefully assess the ability of the CSES orbits and data to provide
59 relevant data for such a purpose. A number of issues are identified, and an appropriate
60 modelling approach is found to mitigate these. The resulting CGGM model appearing to
61 be of high enough quality, it is next used as a parent model to produce a main field
62 model extrapolated to epoch 2020.0, which was eventually submitted on October 1,
63 2019 as one of the IGRF-13 2020 candidate models. This CGGM candidate model, the
64 first ever produced by a Chinese led team, is also the only one relying on a data set
65 completely independent from that used by all other candidate models. A successful
66 validation of this candidate model is performed by comparison with the final (now
67 published) IGRF-13 2020 model and all other candidate models. Comparisons of the
68 secular variation predicted by the CGGM parent model with the final IGRF-13
69 2020-2025 predictive secular variation also reveals a remarkable agreement. This shows
70 that despite their current limitations, CSES magnetic data can already be used to
71 produce useful IGRF 2020 and 2020-2025 secular variation candidate models to
72 contribute to the official IGRF-13 2020 and predictive secular variation models for the
73 coming 2020-2025 time period. These very encouraging results show that additional
74 efforts to improve the CSES magnetic data quality could make these data very useful
75 for long-term monitoring of the main field and possibly other magnetic field sources, in
76 complement to the data provided by missions such as the ESA Swarm mission.

77 **Keywords**

78 CSES, CGGM, IGRF, Geomagnetism, Space magnetometry

79 **Introduction**

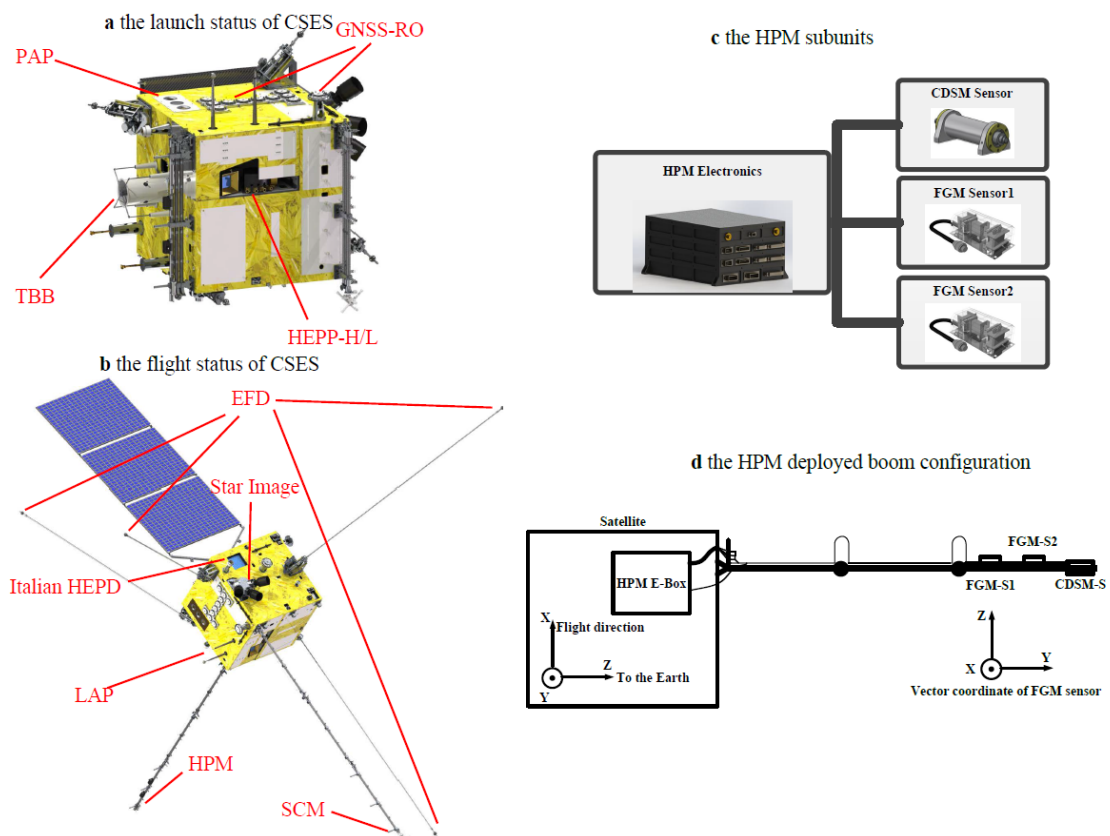
80 The International Geomagnetic Reference Field (IGRF) is a series of mathematical
81 models used to describe the large-scale internal part of the geomagnetic field. The
82 building of these models is an international endeavour carried out under the auspices of
83 the International Association of Geomagnetism and Aeronomy (IAGA). Every five
84 years, these models are updated after IAGA releases an open call to the international
85 community to collect candidate models, which are next assessed and used to build the
86 final official IGRF update (see e.g., [Macmillan and Finlay \(2011\)](#) for more details about
87 IGRF). The previous update (IGRF-12) was published in 2015 ([Thébault et al., 2015a](#))
88 and consisted in a series of snapshot models every five years between 1900 and 2015,
89 and a predictive secular variation model, describing the expected average (linear)
90 temporal variation of the field between 2015 and 2020. A new update (IGRF-13) is now
91 in order, consisting in: 1) replacing the previous 2015 model by an improved 2015
92 model (taking into account data acquired since the last update), 2) providing a new
93 model for epoch 2020, and 3) providing a new secular variation model to describe the
94 expected average (linear) temporal variation of the field between 2020 and 2025. The
95 corresponding call for candidate models has been issued in March 2019 by an IAGA
96 dedicated task force, with an October 1, 2019 deadline.

97 The present paper describes the way one such candidate model for epoch 2020 has
98 been derived (and submitted to the call) using data from the China
99 Seismo-Electromagnetic Satellite (CSES) mission, launched on February 2, 2018 ([Shen
100 et al., 2018](#)). This candidate model, to which we will refer as the CGGM (CSES Global
101 Geomagnetic Field Model) candidate model, is the first ever produced by a Chinese-led
102 team. It also is the first produced by only relying on data from a Chinese satellite. It
103 finally is the only 2020 IGRF candidate model not relying on any data from the ESA
104 Swarm constellation (see [Alken et al., 2020a](#)).

105 The CSES satellite is orbiting on a Sun-synchronous low Earth circular orbit, at an
106 altitude of about 507 km and with an inclination of 97.4°. It has a fixed 14:00 local time

107 (LT) at descending node and a five-days ground track recursive period. Its main
108 scientific purpose is to acquire electric and magnetic field data, as well as plasma and
109 high energetic particles data for the study of signals related to earthquakes, geophysics
110 and space science (see [Shen et al., 2018](#)). Nine payloads are operated on CSES (see
111 Figure 1). Six booms are used, one for the sensors of the High Precision Magnetometer
112 (HPM) payload, one for a Search-Coil Magnetometer (SCM), and four for Electric Field
113 Detectors (EFD). The other six payloads are assembled on the body of the satellite,
114 where a set of three star imagers (STR) is also located to provide attitude restitution.
115 These are a Plasma Analyser (PAP), a Langmuir Probe (LAP), a High Energetic Particle
116 Package from China (HEPP), a High Energetic Particle Detectors from Italy (HEPD), a
117 GNSS Occultation Receiver (GNSS-RO) and a Tri Band Beacon (TBB), the latter being
118 operated in coordination with ground receiver stations in Chinese territory. Generally,
119 except for some individual indicators, all payloads perform very well in orbit and meet
120 their designed technical requirements (e.g., [Yang et al., 2020a](#) and references therein).

121 The main payload of interest for the present study is the HPM ([Cheng et al., 2018](#))
122 used to measure the magnetic field vector and intensity from DC to 15Hz. As shown in
123 Figures 1c and 1d, the HPM consists of two fluxgate magnetometers (FGM-S1 and
124 FGM-S2, to measure the magnetic field vector) and one coupled dark state
125 magnetometer (CDSM, to provide the scalar data for both science applications and
126 calibrations of the FGMs, [Pollinger et al. 2018](#)). All instruments are located on the last
127 leg of a deployable boom with three hinges. FGM-S1 is the nearest to the satellite body
128 (about 3.9 m) and CDSM is the farthest (about 4.7 m). The distance between sensors
129 (FGM-S1 to FGM-S2 and FGM-S2 to CDSM) is about 0.4m. This set-up was chosen to
130 minimize perturbations among instruments and from the satellite body itself. It however
131 has the drawback that the mechanical link between the FGM instruments providing the
132 vector measurements on the boom and the STR providing the attitude restitution on the
133 satellite body is complex and subject to possible deformation along the orbit. As we
134 shall later see, this indeed, is a significant limitation.



135

136 **Figure 1: Configuration of the CSES platform and its payloads.** Left: Launch (a) and
 137 flight (b) configuration of CSES; Right: HPM subunits (c) and deployed boom
 138 configuration (d) with the HPM sensors on the outer segment (Cheng et al., 2018). The
 139 body of the satellite is a 1.4m x 1.4m x 1.5m cube, and the boom (in three segments) is
 140 4.7m long. FGM and CDSM sensors are roughly to scale on the last segment of the
 141 boom in (d).

142 The preparation and production of the CGGM candidate model involved several
 143 steps, and the organisation of the present paper reflects these steps. We first introduce
 144 the characteristics of the CSES HPM data used in this study, as well as that of Swarm
 145 data used in preliminary modelling studies. We next describe early attempts to build
 146 main field models from CSES HPM data, which we compared to main field models
 147 built in a similar way from Swarm data. The purpose of this was to assess if CSES HPM
 148 data were of high enough quality to build a candidate model meeting the standards of
 149 IGRF. This revealed some significant limitations and guided us in our final modelling
 150 strategy. We then move on to describe the way a CGGM parent model was built, first

151 describing the data selection strategy, next describing the model parameterization and
152 optimization strategy, and providing key statistics. We also explain how this parent
153 model was next used to build the CGGM IGRF 2020 candidate model. Finally, we
154 describe the tests we carried out to assess the quality and limitations of this candidate
155 model, and the way we derived realistic uncertainties for each Gauss coefficient. This
156 information was provided with the CGGM candidate model on time for the October 1,
157 2019 deadline. We conclude with an a posteriori assessment of both this CGGM IGRF
158 2020 candidate model and the secular variation associated with the CGGM parent
159 model. This assessment encouragingly reveals that despite their current limitations,
160 CSES data can already be used to produce useful IGRF 2020 and 2020-2025 secular
161 variation candidate models to contribute to the official IGRF-13 2020 and predictive
162 secular variation models for the coming 2020-2025 time period.

163 **Data used in this study**

164 **CSES HPM data**

165 The CSES HPM data that we used are 1Hz level 2 scientific HPM data (version 1.0).
166 The detailed data product contents and instruction for use are to be found in [Yang et al.](#)
167 [\(2020b\)](#). The data are calibrated using the procedure described in [Zhou et al. \(2018\)](#),
168 [Zhou et al., \(2019\)](#), and [Pollinger et al., \(2020\)](#) and provided by the Institute of Crustal
169 Dynamics, China Earthquake Administration. For the purpose of this study, two distinct
170 sets of level 2 data were used, which we will refer to as Type 1 and Type 2 data.

171 Type 1 data are the nominal data of the mission, only provided for CSES geographic
172 locations between 65°S and 65°N (i.e., not at high latitudes). The reason for this is that,
173 as already noted, the CSES mission was not originally intended to provide data for main
174 field modelling. The corresponding 1Hz level 2 data are produced from the original
175 60Hz FGM and 1Hz CDSM data. These data are provided on a half orbit basis and
176 calibrated in several steps (see [Zhou et al. \(2018\)](#), [Zhou et al., \(2019\)](#) and [Pollinger et al.,](#)
177 [\(2020\)](#) for detailed explanations). The FGM (from both FGM, recall Figure 1) and
178 CDSM raw signals are first converted to physical quantity, using calibration parameters

179 determined on ground before the launch of the satellite. The three axes of the two FGMs
180 not being strictly orthogonal, CDSM scalar measurements are next used to calibrate
181 these FGM instruments in orbit, to correct for non-orthogonality, biases and rescale
182 each axis. The corresponding parameters are calculated separately for the day- and
183 night-side and updated every day. Interferences from the satellite and other
184 neighbouring sensors are also further removed. However, occasional significant
185 disturbances from magnetotorquers (MT) and the TBB instrument could not be
186 corrected for. These can be identified from the flags provided with the CSES level 2
187 data and then removed during the data selection. This then leads to scalar data from the
188 CDSM on the one hand, and to calibrated vector data from the FGM-S1 and FGM-S2 in
189 their respective (orthogonalized) instrument reference frames, on the other hand.
190 Although the CSES mission further provides 1Hz Level 2 FGM-S1 and FGM-S2 data in
191 the North East Centre (NEC) reference frame after an additional processing step (see
192 Yang et al., 2020b), we do not use these in our modelling procedure. Rather, we directly
193 take joint advantage of the 1Hz Level 2 FGM data provided in the instrument frame,
194 and of the 1 Hz quaternions describing the rotation to change from the STR reference
195 frame to the Inertial Celestial Reference Frame (ICRF) frame of reference (STR data,
196 also provided as a CSES product).

197 Type 2 data are additional scalar data later made available, motivated by the need to
198 also have access to scalar high-latitude data for the purpose of building a global field
199 model. These additional 1Hz scalar data were only made available for North and South
200 geographic latitudes higher than 65° (and sometimes only at even higher latitudes, see
201 Figure 8 below). They underwent the same calibration procedure as Type 1 data.
202 However, these data not originally being intended to be produced by the CSES mission,
203 they suffer from a number of specific issues. In particular, the way the CSES mission is
204 being operated implies that most magnetically noisy operations and manoeuvres take
205 place during these high latitude orbital segments. In addition, these data were found to
206 suffer from timing inaccuracy. As a result, Type 2 data underwent additional

207 non-nominal dedicated processing, starting from available satellite low-level data and
208 using GPS time to timestamp the data.

209 All data of both types collected in this way were made available to the modelling
210 team, which next screened and selected the data in the way we later describe.

211 **Swarm data**

212 For the purpose of investigating the ability of CSES to provide enough adequate data
213 for building an IGRF model, a number of preliminary tests were done by also using
214 Swarm data. These data were Level 1b 1Hz magnetic data version 0505/0506 from
215 Swarm Alpha between August 01 and September 30, 2018, at a time when this satellite
216 was orbiting at a similar local time as the CSES mission. Note that none of these data
217 were used in the building of the CGGM final parent and candidate models.

218 **Auxiliary data**

219 In addition to the satellite data described above, we also relied on the planetary (3
220 hours) geomagnetic Kp index (see [Bartels, 1949](#) and e.g., [Menvielle and Berthelier,
221 1991](#)), the so-called Ring Current index RC introduced by [Olsen et al. \(2014\)](#), and E_m ,
222 the weighted average over the preceding hour of the merging electric field at the
223 magnetopause (see e.g., [Kan and Lee, 1979](#)).

224 **Early modelling attempts**

225 In the early phase of this study, only Type 1 CSES HPM data were available. These
226 data only cover geographic latitudes between 65°S and 65°N. To be able to build
227 preliminary main field models, it was therefore decided to complement this data set
228 with scalar data from the Swarm Alpha satellite. The goal was to test the value of the
229 Type 1 CSES HPM data for such modelling purposes. The strategy we adopted was to
230 focus on a simple modelling strategy only using two months of data (August-September
231 2018) when CSES Type 1 data were available and Swarm Alpha was orbiting at a
232 similar local time, providing high-latitude scalar data distribution roughly mimicking
233 the scalar data distribution CSES Type 2 data could ultimately provide. The data
234 selection and modelling strategy used was kept simple to match the only two months

235 data availability, and inspired by standard data selection and modelling strategies, such
236 as that used by [Vigneron et al. \(2015\)](#) and [Hulot et al. \(2015a\)](#).

237 **CSES HPM data selection**

238 Only Type 1 CSES HPM data between August 01 and September 30, 2018, were
239 used. 1 Hz scalar data were taken from the CDSM instrument without any geographic
240 restriction (except for the fact, of course that no Type 1 CSES HPM data were available
241 at high geographic latitudes beyond 65°S and 65°N). Since FGM-S2 was further away
242 from the satellite body (see Figure 1), Type 1 CSES HPM data from this instrument
243 were initially assumed to be of the best quality (rather than FGM-S1), and thus selected
244 for providing the needed 1 Hz vector data (expressed in the instrument's reference
245 frame). These were further selected according to Quasi-Dipole (QD) latitude ([Richmond,
246 1995](#)), using two alternative choices (for testing purposes). A first selection involved
247 selecting vector data at QD latitudes between -55° and +55° (to which we will refer as
248 the 55°QD selection). A second selection involved selecting vector data at QD latitudes
249 between -20° and +20° (to which we will refer as the 20°QD selection). To avoid
250 spurious data (due to interference by e.g., the TBB instrument) all vector and scalar data
251 were also screened to ensure that no scalar data (or modulus of the vector data) departed
252 from predictions by the CHAOS-6-x8 model (latest version of the CHAOS-6 model of
253 [Finlay et al. \(2016\)](#) available at the time) by more than 300 nT. Such pre-screening of
254 data using a reasonable prior model is standard practice (see e.g., [Finlay et al., 2016](#);
255 [Vigneron et al., 2015](#); [Hulot et al., 2015a](#)) to remove the relatively few most obvious
256 outliers without biasing the bulk of the data towards the chosen prior model (the choice
257 of the 300 nT ensuring this). In addition, for both vector and scalar data, only night side
258 data were used, using classical criteria to avoid perturbations due to external sources
259 (LT between 18:00 and 06:00, $K_p < 2+$, $RC < 2$). Finally all data were decimated (one
260 point every two minutes) to avoid noise correlation between consecutive data and
261 oversampling along the satellite track, while keeping enough data, given the targeted
262 level of modelling.

263 **Swarm Alpha data selection**

264 Swarm Alpha data were used for two different purposes. The first was to provide the
265 scalar data at QD latitudes poleward of $\pm 55^\circ$ needed to complement the Type 1 CSES
266 HPM data to be able to produce main field models. This first set of data was selected
267 according to the same criteria as the Type 1 CSES HPM data, further requesting that
268 $E_m < 10\text{mV/m}$, and decimated in the same way.

269 The second purpose was to provide additional data for building reference models
270 entirely based on Swarm data, over the same August to September 2018 time period,
271 sharing similar local time properties and selection criteria as the CSES data. In addition
272 to the previous high QD latitudes scalar data, two additional Swarm Alpha data sets
273 were thus prepared, including 1Hz scalar and vector data (expressed in the Swarm
274 Alpha VFM vector field magnetometer reference frame) and selected according to
275 similar criteria as either the 55°QD selection (first data set) or the 20°QD selection
276 criteria (second data set) described above for the CSES HPM data. These data were
277 again decimated in the same way.

278 **Model parameterization and optimization**

279 Model parameterization was chosen to be the same for the four models we derived in
280 this preliminary series of tests (one CSES model and one Swarm model for each 55°QD
281 or 20°QD data selection). This parameterization is a simplified version of that used by
282 [Vigneron et al. \(2015\)](#) and [Hulot et al. \(2015a\)](#). Simplification involved parameterizing
283 the main field only up to spherical harmonic (SH) degree and order 15, and only
284 allowing for a linear secular variation (SV) up to degree and order 5. This maximum
285 degree was chosen to account for the fact that only two months of data were considered,
286 and that changes in the field due to higher degree SV during such a short period are
287 below the resolution of the data and cannot be resolved. No special procedure was used
288 to handle the crustal field signal above degree 15 (which is neither modelled, nor
289 removed), since this signal also appears to mainly be beyond recovery with just two
290 months of data. To describe the external (magnetospheric) and corresponding

291 Earth-induced fields, we mainly followed the CHAOS-4 model parameterization (Olsen
 292 et al., 2014, also used by Hulot et al., 2015a.). In practice, however, only simplified
 293 parameters to account for the remote magnetospheric sources and the near
 294 magnetospheric ring current were included. Using the notation of Olsen et al. (2014, see
 295 their equations 4 and 5), remote magnetospheric sources (and their induced
 296 counterparts) are thus described by a zonal external field up to degree 2 in geocentric
 297 solar magnetospheric (GSM) coordinates (2 coefficients, $q_1^{0,GSM}$ and $q_2^{0,GSM}$), while the
 298 near magnetospheric ring current (and its induced counterpart) is described by using
 299 solar magnetic coordinates (SM, see Hulot et al., 2015b, for definitions of the GSM and
 300 SM coordinate systems, and Maus and Luehr, 2005 for the justification of such an
 301 approach). However, only a static field up to degree 2 (Δq_1^0 , Δq_1^1 , Δs_1^1 , q_2^0 , q_2^1 , q_2^2 , s_2^1 ,
 302 s_2^2) and a time-varying part proportional to the RC index for degree 1 (\hat{q}_1^0 , \hat{q}_1^1 , \hat{s}_1^1) is
 303 assumed, leading to 11 parameters in total. Finally, only one set of Euler angles
 304 (assumed static throughout the two months time period considered) was also solved for
 305 to recover the unknown rotation between the vector instruments (FGM-S2 for CSES,
 306 VFM for Swarm) and the STR data provided by each mission. This choice was intended
 307 for potential issues with the stability of this rotation to best manifest themselves in the
 308 data residuals (see Figures 6 and 7 and later discussion). In total, 306 parameters were
 309 thus solved for, 255 for the static Gauss coefficients, 35 for the linear SV, 13 parameters
 310 for the external field, and 3 for the Euler angles.

311 For solving the inverse problem, we relied on an iteratively reweighted least-squares
 312 algorithm with Huber weights (as in Olsen et al., 2014, see also e.g., Farquharson and
 313 Oldenburg 1998). The cost function to minimize is $e^T C^{-1} e$, where $e = d_{obs} - d_{mod}$
 314 is the difference between the vector of observations d_{obs} (in the reference frame of the
 315 instrument) and the vector of model predictions d_{mod} , and C is the data covariance
 316 matrix (updated at each iteration). No regularization was applied, but a geographical
 317 weight was introduced, proportional to $\sin(\theta)$ (where θ is the geographic co-latitude),
 318 to balance the geographical sampling of data. Both scalar data and Huber weights make

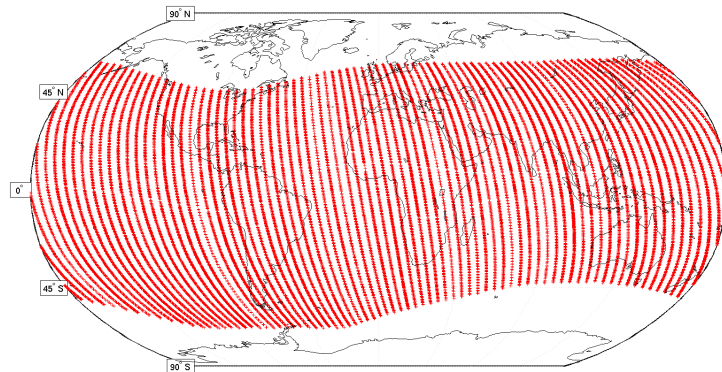
319 the cost function nonlinearly dependent on the model parameters. The solutions were
320 therefore obtained iteratively, using a Newton-type algorithm.

321 A priori data error standard deviations were set to 2.5 nT for both scalar and vector
322 data in all cases (Swarm and CSES data). Attitude error was assumed isotropic (using
323 the formalism of [Holme and Bloxham \(1996\)](#)). Different values were chosen for CSES
324 (100 arcsecs) and Swarm (10 arcsecs), however. A much higher value was indeed
325 required for CSES to account for the significantly lower quality of the mechanical link
326 between the CSES STR reference frame and FGM reference frame (see below).

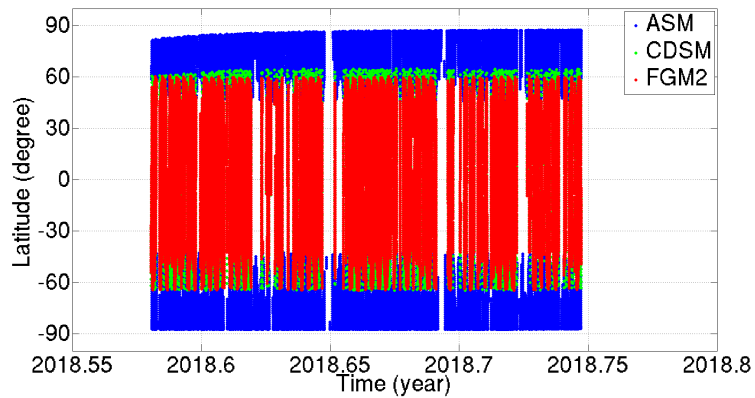
327

328

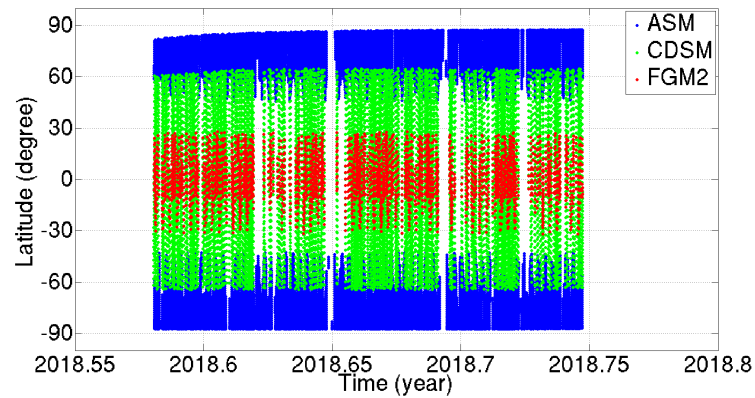
329



330

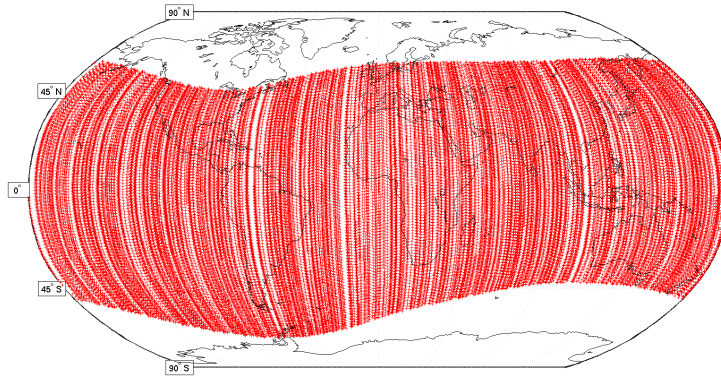


331

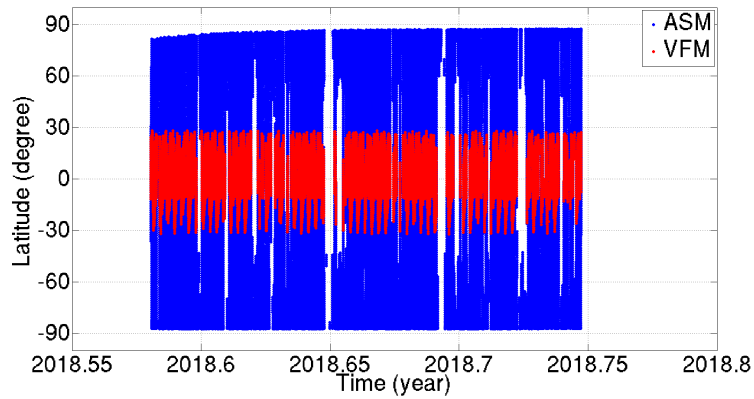
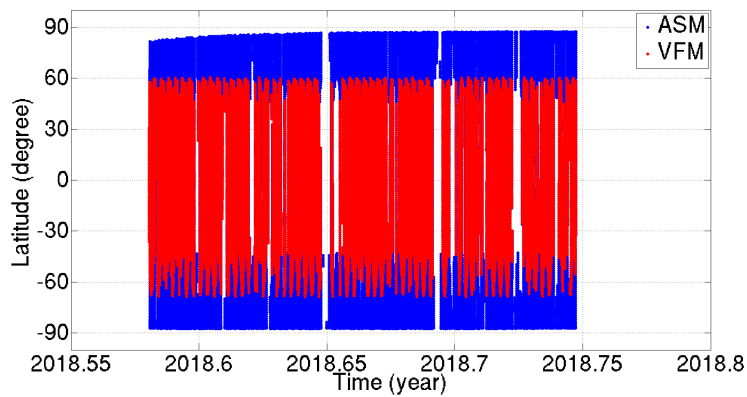


332 **Figure 2: CSES data distribution (complemented with high latitude Swarm scalar**
333 **data) used for preliminary modelling attempts. Top: geographic distribution of the**
334 **QD55° CSES vector data selection; Middle: Latitude versus time distribution of the**
335 **QD55° data selection; Bottom: Latitude versus time distribution of the QD20° data**
336 **selection. In all plots, red for CSES (FGM_S2) vector data, green for CSES (CDSM)**
337 **scalar data, blue for complementary Swarm Alpha scalar data.**

338



339



340

341 **Figure 3: Swarm Alpha data distribution used for preliminary modelling attempts.**

342 *Top: geographic distribution of the Swarm Alpha QD55° vector data selection; Middle:*

343 *Latitude versus time distribution of the QD55° data selection; Bottom: Latitude versus*

344 *time distribution of the QD20° data selection. In all plots, red for vector data, blue for*

345 *scalar data.*

346

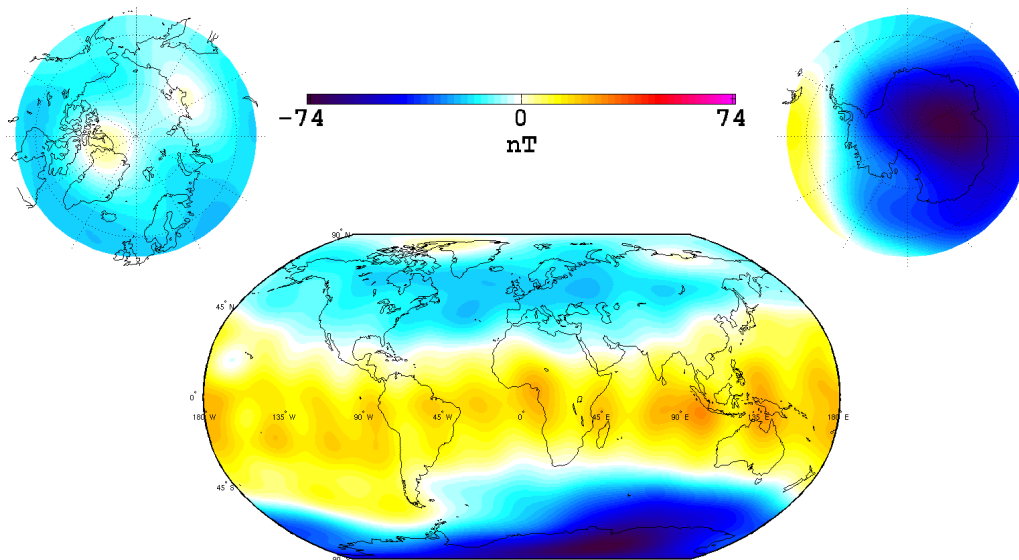
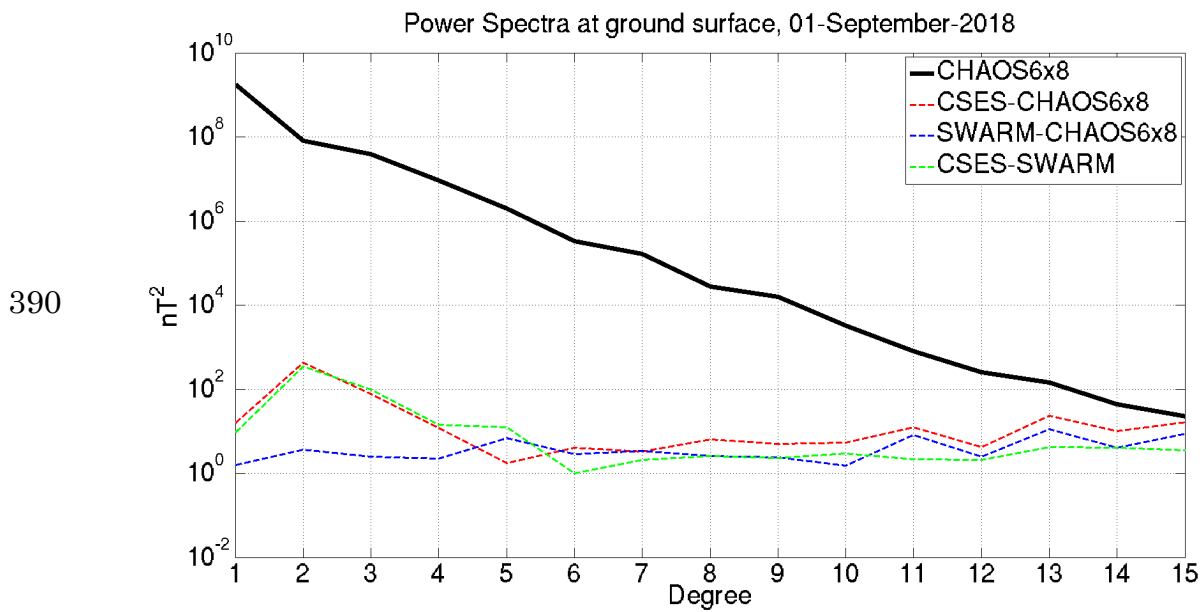
347 **Lessons learnt**

348 Four models were produced in total. Two were built using the Type 1 CSES HPM
349 vector and scalar data from either the 55°QD or the 20°QD selection, complemented
350 with high latitude Swarm Alpha scalar (as described above). For brevity, we will refer
351 to these as the 55°QD and 20°QD CSES models. Two additional Swarm reference
352 models were otherwise built in the same way, using the 55°QD and 20°QD Swarm data
353 selections (55°QD and 20°QD Swarm models). Figures 2 and 3 illustrate the
354 corresponding data distributions. Comparing Figures 2a and 3a (availability of vector
355 data between -55° and +55° QD latitudes from respectively CSES and Swarm Alpha)
356 reveals a significant difference between the CSES and Swarm data distributions.

357 Whereas the Swarm Alpha orbit provides a nice global coverage of all longitudes
358 over the two months considered, the five days revisiting period of CSES is responsible
359 for a significantly poorer longitudinal distribution, leaving roughly 80 sectorial gaps.
360 But we note that by the Nyquist sampling criterion, 80 equally spaced bands in
361 longitude should allow the recovery of sectorial dependence up to order 40. These gaps
362 are thus expected to be narrow enough to only mildly affect the recovery of a global
363 field model up to degree and order 15. Indeed, this does not turn out to be the most
364 significant issue.

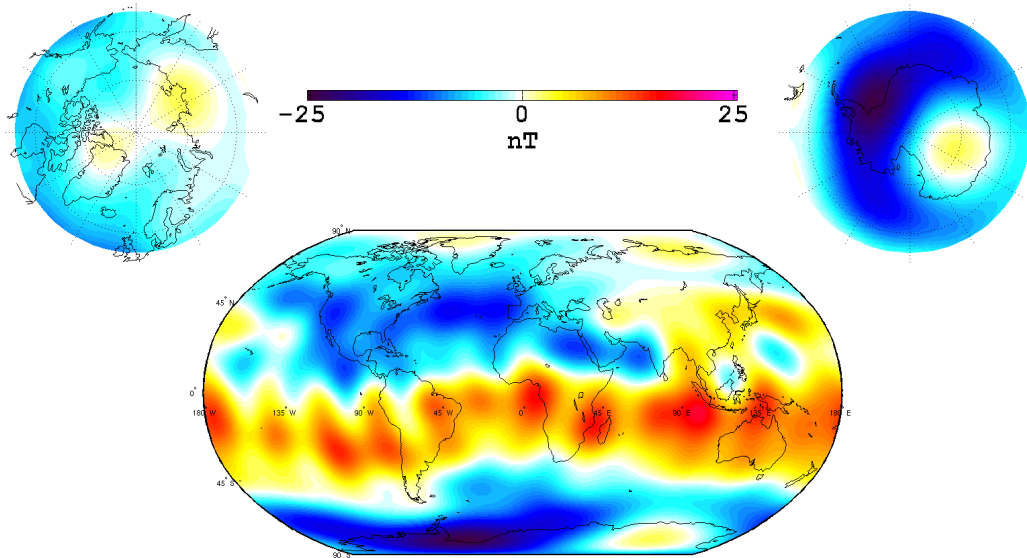
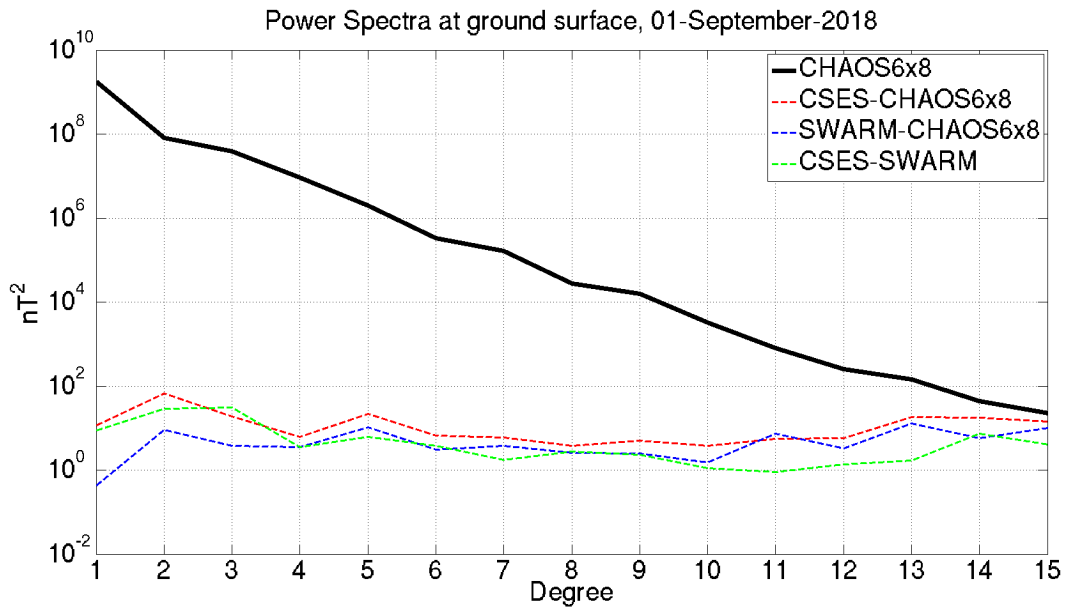
365 A much more significant issue is revealed by the comparison of the CSES and
366 Swarm 55°QD models, as shown in Figure 4. For SH degrees 1 to 4, the
367 Lowes-Mauersberger spatial spectrum (Mauersberger, 1956; Lowes, 1966) of the
368 differences between these two models at the Earth's surface for central epoch of the
369 models (September 1, 2018) is clearly much larger than that of the differences between
370 the Swarm 55°QD model and the CHAOS-6-x8 model for the same epoch. The latter
371 spectrum provides a good indication of the limitation of using only two months of
372 55°QD selected data from a single satellite. Clearly, the CSES 55°QD model fails to
373 properly determine the first four spherical harmonic degrees of the field. Plotting the
374 radial component of the difference between the predictions of the CSES and Swarm

375 55°QD models at the Earth's surface (also shown in Figure 4) makes it clear that this
376 disagreement, reaching up to 70 nT at Earth's surface, is mainly zonally distributed and
377 not related to the sectorial gaps seen in Figure 2. Its magnitude also makes it difficult to
378 relate to differences in the magnetic field signals seen by the Swarm and CSES satellites,
379 which share similar altitudes, or to some potentially poorly recovered secular variation,
380 which cannot produce such differences between models built with only two months of
381 data. Although one cannot exclude that this disagreement could be due to some other
382 unidentified issue, the most likely possibility we identified is related to the mechanical
383 link between the FGM_S2 instrument (on the last leg of the boom, see Figure 1) and the
384 STR (providing attitude information, but located on the body of the satellite). This link
385 is prone to potential systematic deformation along the orbit. Recall indeed that our
386 modelling procedure assumes this link to be strictly rigid throughout the two months
387 period considered, whereas the design of the CSES HPM boom (three segments with
388 three hinges) may not be capable of guaranteeing this.
389



391
 392 **Figure 4: CSES and Swarm 55°QD model comparison.** Top: Lowes-Mauersberger
 393 spatial power spectra of the CHAOS-6-x8 model (black), of the difference between the
 394 CSES 55°QD and CHAOS-6-x8 models (red dashed), of the difference between the
 395 Swarm 55°QD and CHAOS-6-x8 models (blue dashed), and of the difference between
 396 the CSES 55°QD and Swarm 55°QD models (green dashed); Bottom: Radial
 397 component of the difference between the predictions of the CSES and Swarm 55°QD
 398 models; All plots for central epoch September 1, 2018 and at Earth's surface.

399



400

401 **Figure 5: CSES and Swarm 20°QD model comparison.** Same plotting convention as in
402 Figure 4 (except for scaling in bottom plot), using CSES and Swarm 20°QD models
403 instead of CSES and Swarm 55°QD models.

404

405 To check this possibility and attempt to improve the quality of the CSES model to be
406 recovered, we relied on similar comparisons, now using the CSES and Swarm 20°QD
407 models. These models are based on much less vector data, all concentrated in a 40° QD
408 wide equatorial band along the magnetic equator. The hope was that the mechanical link
409 (rotation matrix) between the FGM_S2 and STR frames of reference would be stable
410 enough along this equatorial part of the (night-side) orbit leg, and similar enough from
411 one orbit to the next, to behave as if almost stiff. Ignoring all vector data was obviously
412 not an option, since enough vector data close to the magnetic equator are mandatory, in
413 particular to provide the knowledge of where this equator lies, a critical information
414 (see [Khokhlov et al., 1997, 1999](#)) to avoid the recovered model being affected by the
415 so-called Backus effect ([Backus, 1970](#), also known as the perpendicular effect, [Loves,](#)
416 [1975](#)). Figure 5, to be compared to Figure 4, shows that this indeed brings improvement.
417 The disagreement between the two CSES and Swarm 20°QD models for degrees 1 to 4
418 is much reduced. The reduced use of vector data comes at a slight cost, though, with a
419 modest degradation of the recovery of the degree 5 SH component (see also the impact
420 on the Swarm 20°QD model when compared to the CHAOS-6-x8 model). Overall,
421 nevertheless, the improvement is very substantial, as can also be seen in the map of the
422 radial component of the difference between the predictions of the CSES and Swarm
423 20°QD models plotted at the Earth's surface (also shown in Figure 5). Although the
424 zonal effect is not entirely removed, it now leads to disagreements about three times less
425 in magnitude, only reaching 25 nT at most at Earth's surface (note the difference in the
426 colour scales used in Figures 4 and 5).

427 To further confirm that the issue in the CSES models is indeed likely linked to some
428 deformation of the boom along the orbit, we finally computed the residuals between the
429 CSES Type 1 vector data used and the predictions of the CHAOS-6-x8 model (which
430 includes both internal and magnetospheric source contributions, but not, e.g., in-situ
431 ionospheric currents crossed by the satellite). Should the CSES vector data be free of
432 any slowly varying biases (such as produced by orbital boom deformation), these

433 residuals would be expected to only reflect noise in the data and contributions of signals
434 from sources not modelled by CHAOS-6-x8. In contrast, if boom deformation occurs
435 systematically along the orbit, significant signatures would be expected in the form of
436 slowly varying biases as a function of latitude. Since it is known that no such effect is to
437 be found on Swarm Alpha (see e.g., [Olsen et al. 2015](#); each Swarm satellite has its VFM
438 rigidly linked to its set of STR on a specially designed optical bench), a simple way to
439 check this is to plot the equivalent residuals between the Swarm Alpha vector data and
440 predictions of the CHAOS-6-x8 model. Both satellites orbiting at the same local time
441 over the time period considered (therefore sensing similar un-modelled sources), the
442 latter residuals are expected to provide a relevant baseline.

443 Residuals were computed in both the NEC and instrument frames of reference,
444 taking advantage of the Euler angles computed in the course of producing the 55°QD
445 CSES and Swarm models to convert vector components from one frame to the other.
446 Residuals in the NEC frame were computed using the Euler angles and quaternion
447 information to rotate the vector data from the instruments frame to the NEC frame,
448 before subtracting the predictions of the CHAOS-6-x8 model (Figure 6). Residuals in
449 the instruments frame were computed using the quaternion information and Euler angles
450 to rotate the predictions of the CHAOS-6-x8 model before subtracting these from the
451 vector data (Figure 7).

452 As can be seen, no significant bias can be found in the Swarm Alpha residuals,
453 which also display a dispersion of the type expected for Swarm, for the quiet night time
454 selection used in this study (see e.g., [Olsen et al., 2015](#)). In contrast, strong varying
455 biases can be found in the CSES residuals. These biases are strongest in the high
456 southern latitudes, progressively decrease towards the equator, and are much less
457 marked in the northern hemisphere. This North-South asymmetry, we note, is consistent
458 with a similar asymmetry in the disagreements between the CSES and Swarm models
459 (stronger in the Southern hemisphere than in the Northern hemisphere, recall Figures 4
460 and 5). Since CSES orbits at a fixed 14h00 LT at descending node, this evolution

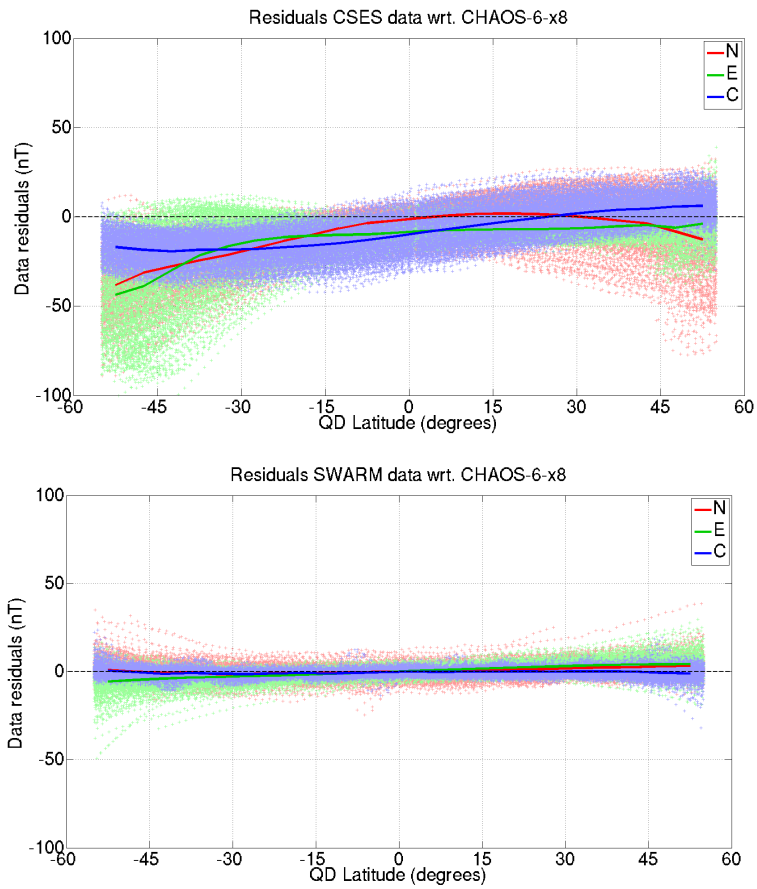
461 follows the path of the satellite on its night leg of the orbit, from South to North. It
462 shows that the bias is maximum every time CSES moves away from the Sun at the end
463 of the dayside orbit leg during which the boom has been presumably heated, than starts
464 decreasing as the satellite begins its journey northwards in the dark, allowing the boom
465 to progressively cool down. This thus strongly suggests that the bias signature is indeed
466 related to some thermal boom deformation, which builds up on the dayside leg of the
467 orbit, then thermally relaxes on the night side leg, settling back to a roughly stable state
468 by the time the satellite reaches the equator on this night side. This evolution also shows
469 that the most problematic CSES vector data are those from the southernmost part of the
470 (night-side) orbit. These data being dismissed in the QD20° data selection, it naturally
471 explains why the 20°QD CSES model appears to be of much better quality than its
472 55°QD equivalent.

473 Last but not least, Figures 6 and 7 also clearly show that the dispersion in the CSES
474 residuals is much larger than that in the Swarm Alpha residuals. It is highly doubtful
475 that this could be the result of different natural un-modelled signals seen by the two
476 satellites. The intrinsic noise level affecting the FGM_S2 measurements (due to the
477 instrument, the satellite and the rest of the payload) having been shown to be roughly
478 comparable to that affecting the Swarm Alpha VFM instrument (Zhou et al., 2019), this
479 we practically attributed to the impact of the not-so-stiff boom and possibly also errors
480 in the attitude restitution provided by the STR through the quaternions (though
481 independent checks of these STR data, not reported here, suggest that this source of
482 error is much less significant, except possibly on some specific days, see below). This
483 noise level is the reason we assumed a fairly large error of 100 arsecs for the attitude
484 when computing CSES models.

485 A number of important lessons were thus learnt from the above preliminary
486 modelling attempts. One is that the a priori unfavourable 5 days recursive period of
487 CSES, which introduces longitudinal gaps in the data distribution (see Figure 2), does
488 not appear to be critical for IGRF modelling purposes. Another one, unfortunately much

489 more critical, is that the mechanical link between the FGM (on the last leg of the three
490 hinges boom) and the STR (on the body of the satellite) appears to be problematic. The
491 boom seems to suffer from systematic thermal deformations along the orbit of CSES,
492 which affect the recovery of the attitude of the vector data provided by the FGM. This
493 deformation could be roughly characterized, and the issue appears to mainly affect data
494 from the southernmost part of the night side leg of the CSES orbits needed for IGRF
495 modelling purposes. Nevertheless, a simple workaround could be found, which
496 consisted in selecting vector data only within a 40° QD band centred on the magnetic
497 equator (the 20° QD selection), and assuming an attitude error of 100 arcsecs in the
498 inversion procedure. The timeline imposed by the IGRF deadline of October 1, 2019,
499 did not allow us to test more advanced strategies, and this is the strategy we therefore
500 used to also produce the CGGM parent model as described below. One significant
501 change we made, however, is that we decided not to use the vector data provided by the
502 FGM_S2 instrument, in favour of the vector data provided by the FGM_S1 instrument.
503 This choice was justified by the fact that this instrument being closer to the satellite
504 (recall Figure 1), boom deformation can be expected to be slightly attenuated, with the
505 potential drawback of having slightly noisier data (because of the smaller distance to the
506 satellite) being minor, since such noise level has not been identified as the limiting
507 factor.
508

509

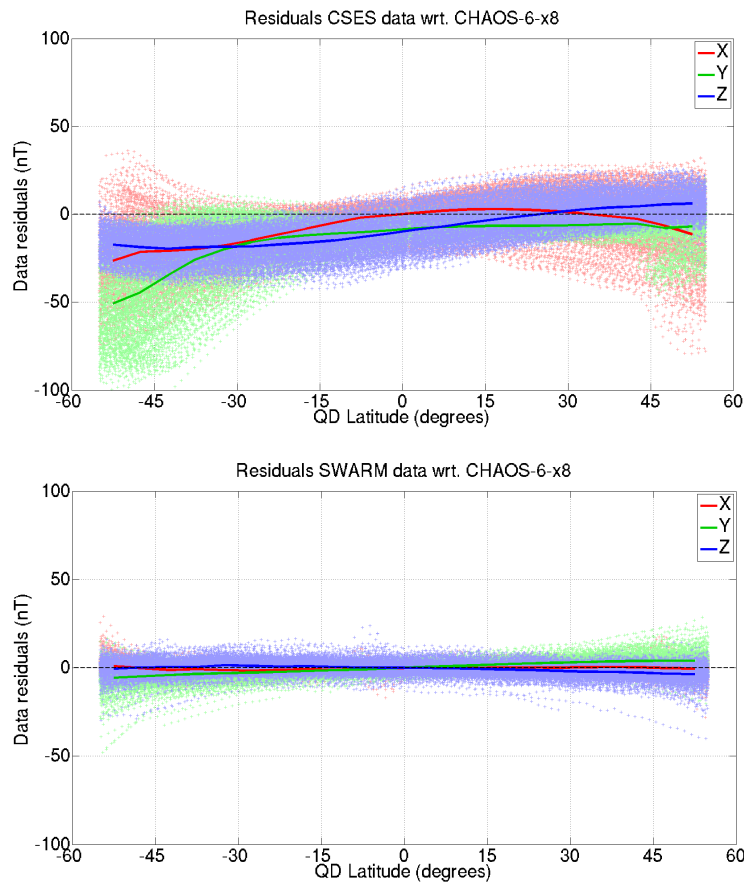


510

511 **Figure 6: CSES (top) and Swarm Alpha (bottom) vector data residuals plotted in the**
512 **NEC frame, as a function of QD latitude, after subtraction of predictions of the**
513 **CHAOS-6-x8 model (including magnetospheric contributions). Red for North; green for**
514 **East; blue for Center. Solid lines show the average of all orbits.**

515

516



517

518 **Figure 7: CSES (top) and Swarm Alpha (bottom) vector data residuals plotted in the**
519 **instruments frame (FGM_S2 for CSES and VFM for Swarm Alpha), as a function of**
520 **QD latitude, after subtraction of predictions of the CHAOS-6-x8 model (including**
521 **magnetospheric contributions). Red for the X component; green for the Y component;**
522 **blue for the Z component. Note that these components are defined differently for the**
523 **FGM_S2 and VFM instruments and may not be directly compared (component to**
524 **component), contrary to the North, East, Centre components shown in Figure 6. Solid**
525 **lines show the average of all orbits.**

526 **CGGM parent model and IGRF 2020 candidate model** 527 **construction**

528 We now move to the description of the way the CGGM parent model was built and
529 next extrapolated in time to build the CGGM IGRF 2020 candidate model, taking
530 advantage of the lessons learnt during our early modelling attempts, and of a
531 much-increased amount of data. The CGGM parent model covers a longer time period
532 and uses all CSES data available before the October 1, 2019 deadline. It also only uses
533 CSES data, Type 2 scalar data covering high latitudes having been made available on
534 time by CSES team for this purpose, to avoid having to rely on any Swarm (or other
535 satellite) data, in contrast to what had been done for the previous preliminary modelling
536 attempts. It finally uses a slightly more advanced data selection and modelling strategy
537 (closer to that used by [Hulot et al., 2015a](#)) to reach the quality needed to next extract an
538 IGRF 2020 candidate model meeting the requirements of the call.

539 **Data selection**

540 *Temporal coverage*

541 Data used (both Type 1 and Type 2) now cover almost 19 months, between March 03,
542 2018 and September 20, 2019.

543 *Geographic coverage*

544 1 Hz scalar data (both Type 1 and Type 2) were taken from the CDSM instrument
545 without any geographic restriction. 1 Hz vector data (only Type 1) were taken from the
546 FGM_S1 instrument (expressed in the instrument's reference frame) selected according
547 to the 20°QD selection, i.e., only within the -20°QD to 20°QD equatorial band.

548 *Selection criteria common to both scalar and vector data*

549 Quality check: Removal of data not satisfying the criteria that differences between
550 each datum and the prediction from the CHAOS-6-x9 model (latest version of the
551 CHAOS-6 model of [Finlay et al. \(2016\)](#), which had then been made available) should
552 be less than 100 nT (scalar or norm comparison for vector data). This more stringent
553 criterion was found to be better suited to remove the occasional blatant outliers who are

554 slightly more numerous within the 100nT-300nT range in the Type 2 data (which were
555 not used in the preliminary study).

556 Night-time selection: Sun angle seen by the satellite required to be at least 10° below
557 horizon for night-time selection (rather than LT selection, as was done for the
558 preliminary models). This ensures better night-time selection and was found to be
559 compatible with the available Type 2 data.

560 Magnetically quiet conditions: based on $|dRC/dt| < 2\text{nT/h}$ and $Kp < 2+$.

561 *Additional selection criteria for scalar data*

562 A more stringent $E_m < 0.8\text{ mV/m}$ criterion than for the preliminary models was
563 required for high latitude scalar data. This was again found to be compatible with the
564 available Type 2 data. A dedicated Flag signalling when magnetotorquers were
565 activated on CSES was provided with the data and used to avoid data at times of
566 magnetotorquer activation for all Type 1 data (Flag MT should be 0). This flag was not
567 used for Type 2 data, as magnetotorquers are activated most of the time at high latitudes
568 (as a result of the operating mode of the satellite). These perturbations however remain
569 within 20 nT for these Type 2 data. Finally, decimation was applied to Type 1 data to
570 avoid over-representation along tracks, but not to the much scarcer Type 2 data. That
571 led to scalar data (for both Types 1 and 2 data) typically separated by one minute.

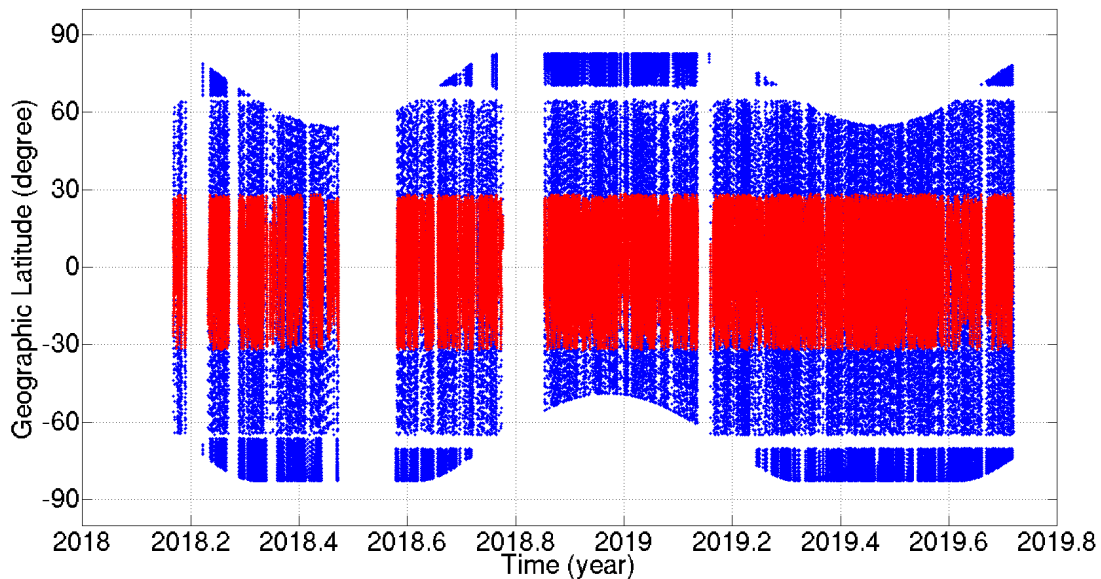
572 *Additional selection for vector data:*

573 Scalar residuals (difference between scalar provided by CDSM and modulus of
574 vector provided by FGM_S1) were required to be less than 2.5 nT. In addition, 17 days
575 of problematic vector data were discarded: 15 days in 2018 (May 4, 8, 12, 14, 18, 20, 27,
576 29-31; June 5, 12-14 ; September 24) and 2 days in 2019 (March 3, September 20).
577 Given the selection criteria previously applied to the data, the issue during these days is
578 most likely due to temporary problems with attitude restitution, leading these data to be
579 incompatible with the rest of the dataset (recall indeed that we do not apply any specific
580 selection criteria on STR data). Finally, decimation was also applied (now keeping 1
581 point out every 15s) to again avoid over-representation along track.

582 *Total amount of data selected:*

583 Overall, this selection procedure resulted in the selection of 92 068 scalar data
584 (among which 62 715 data at absolute geographic latitudes higher than 65°) and
585 122 867 x 3 vector data, distributed in time and latitude as illustrated in Figure 8.

586



587

588 *Figure 8: Latitude versus time distribution of the selected CSES data used for*
589 *building the CGGM parent model (red: FGM_S1 vector data; blue: CDSM scalar data,*
590 *note the gaps around $65^\circ N$ and $65^\circ S$ due to unavailability of CDSM data in this*
591 *transition from Type 1 to Type 2 data available at the time of modelling).*

592

593 **CGGM parent model parameterization and optimization**

594 The model parameterization we chose to build the CSES parent model with is more
595 sophisticated than the one used for the preliminary modelling attempts, given the longer
596 time period to be modelled. It now is closer to that used by [Hulot et al. \(2015a\)](#). The
597 main field is still modelled up to SH degree and order 15, but the linear SV is now
598 modelled up to degree and order 8. As before (and again referring to the notation of
599 [Olsen et al., 2014](#)), the remote magnetospheric sources (and their induced counterparts)
600 are described by a zonal external field up to degree 2 in GSM coordinates (2

601 coefficients) while the near magnetospheric ring current (and its induced counterpart) is
602 described by an external field up to SH degree and order 2 in SM coordinates. The latter,
603 however, is now modelled in a more advanced way. SH degree 2 coefficients are still
604 assumed static (5 coefficients $q_2^0, q_2^1, q_2^2, s_2^1, s_2^2$). SH degree 1 coefficients are still
605 described by a fast time varying part proportional to the RC index for degree 1 (3
606 coefficients $\hat{q}_1^0, \hat{q}_1^1, \hat{s}_1^1$), but their baselines are no longer assumed static. For the zonal
607 coefficient, Δq_1^0 is now allowed to change every 5 days (since 98 time segments of 5
608 days are involved, this implies solving for 98 different coefficients), while for the
609 sectorial coefficients, Δq_1^1 and Δs_1^1 are now allowed to change every 30 days
610 (implying solving for $2 \times 19 = 38$ different coefficients). Finally, Euler angles are now
611 also allowed to change every ten days, to account for possible long-term deformation of
612 the mechanical link between the FGM_S1 instruments and the STR (implying solving
613 for $3 \times 53 = 159$ different coefficients). In total, 640 parameters were thus solved for, 255
614 for the static Gauss coefficients, 80 for the linear SV, 146 parameters for the external
615 field, and 159 for the Euler angles.

616 For solving the inverse problem, we relied on the same iteratively reweighted
617 least-squares algorithm with Huber weights as for the preliminary models (again with
618 no regularization, and using the same geographical weight). A priori data error standard
619 deviations were slightly reduced to 2.2 nT for both scalar and vector data. Attitude error
620 was again set to 100 arcsecs. For completeness, we also specify that CHAOS-4 (Olsen
621 et al., 2014) up to degree and order 13 for epoch 01/03/18 was used as a (static) starting
622 model for the iterative computation. This choice was made to ensure faster convergence
623 of the iterative computation than just starting from a simple dipole field. It has been
624 shown to have very little influence on the final model (see e.g., Vigneron et al., 2015).
625 Full convergence of the computation was then reached after eight iterations. Resulting
626 residual statistics (using the same conventions as in Hulot et al., 2015a) are provided in
627 Table 1.

628

Residual statistics of the CGGM parent model			
	N	Mean (nT)	RMS (nT)
F_P	30246	-0.02	6.20
$F_{NP} + B_B$	184689	+0.29	2.60
$F + B_B$	214935	+0.26	3.16
B_B	122867	+0.47	2.67
B_r	122867	+0.06	8.08
B_θ	122867	-0.70	4.84
B_ϕ	122867	+0.05	5.57

630

631 **Table 1: Residual statistics for all data used to produce the CGGM parent model**
632 *(using the same convention as in [Hulot et al., 2015a](#)). For each type of data, N is the*
633 *number of data used, while Mean and RMS are the Huber-weighted misfit mean and*
634 *Root Mean Square values (in nT); F_P refers to the misfit of the scalar data above*
635 *(absolute) QD latitude 55° (polar latitudes), F_{NP} to the misfit of the scalar data below*
636 *(absolute) QD latitude 55° (non-polar latitudes), F to the misfit of all scalar data, B_B to*
637 *the misfit of the field component projected along the field direction (providing a*
638 *measure of the misfit of the modulus of the vector data with respect to model prediction)*
639 *and B_r , B_θ and B_ϕ refer to the three geocentric vector field components. Note that*
640 *vector residuals provided here are reconstructed residuals propagated from the vector*
641 *residuals minimized in the reference frame of the instrument. Recall that vector data are*
642 *only used for (absolute) QD latitude below 20° .*

643

644 **CGGM IGRF 2020 candidate model generation**

645 The CGGM parent model provides a spherical harmonic estimate of the main field
646 up to degree and order 15 for central epoch December 11, 2018, together with a
647 spherical harmonic estimate of the average secular variation over the time covered by
648 the data (March 2018 to September 2019) up to degree and order 8.

649 The CGGM IGRF 2020 candidate model was simply extrapolated in time from the
650 CGGM parent model up to degree and order 13, using the central epoch December 11,
651 2018 as initial point and the SV coefficients up to degree and order 8 to extrapolate the
652 model to epoch January 1, 2020. No temporal extrapolation for spherical harmonic with
653 degrees 9 to 13 was used (which were thus assumed identical to that inferred by the
654 CGGM parent model for central epoch December 11, 2018). Although this will have
655 undoubtedly introduced some additional source of error in the CGGM candidate model,
656 this choice was made to keep with our original goal of building an IGRF candidate
657 model entirely, and only, based on CSES data.

658 **Initial quality assessment**

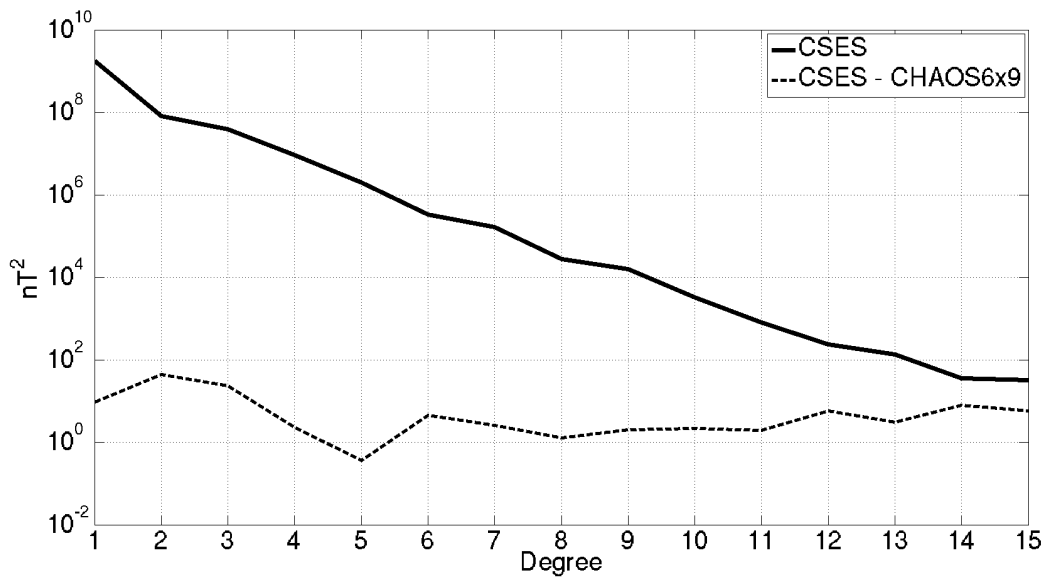
659 To validate the CGGM candidate model, we relied on some comparison of the
660 predictions of the CGGM parent model with those of the CHAOS-6-x9 model. This
661 CHAOS-6-x9 model was computed by DTU only using L1b Swarm data (plus data
662 from earlier missions as well as data from ground observatories) and is therefore
663 independent from the CGGM parent model (except, strictly speaking, for the very minor
664 fact that data used for producing the CGGM parent model were first checked against the
665 this CHAOS-6-x9 model for rejecting very occasional extreme outliers). But since it
666 only uses data up to April 2019, a comparison of predictions for epoch 2020.0 was not
667 considered appropriate. In contrast, CHAOS-6-x9 could be considered to provide a very
668 reliable estimate of the main field for two epochs of interest, December 11, 2018, which
669 corresponds to the central time of the CGGM parent model, and November 20, 2017,
670 which is 103 days before the very first data used to build the CGGM parent model. This
671 is the same amount of time separating the last data used in the CGGM parent model and

672 epoch 2020.0. Given the symmetry of the CSES data distribution we used (recall Figure
673 8), we considered this backward extrapolation test as a good way to assess how well our
674 CGGM IGRF 2020.0 candidate model could be expected to perform.

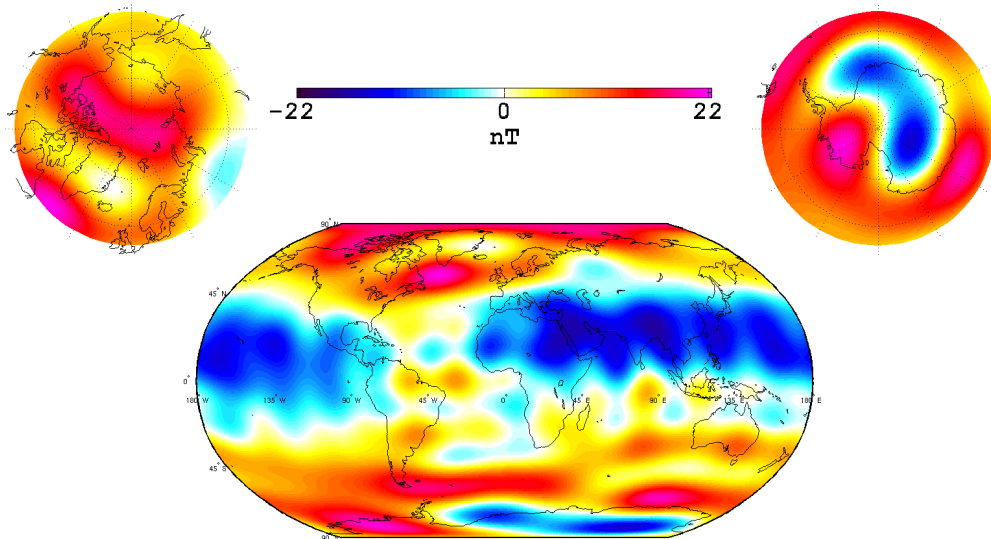
675 Figure 9 illustrates the differences between the CGGM parent and CHAOS-6-x9
676 models at Earth's surface, for central epoch December 11, 2018. The radial component
677 B_r of the difference between the two models reveals a mainly zonal signature, with
678 amplitudes reaching 22nT. These differences are reminiscent of those we had found in
679 our early modelling attempts when comparing CSES based and Swarm Alpha based
680 models, but appear to be slightly weaker (recall Figure 5), despite the fact that we now
681 also only use CSES (Type 2) scalar data at high latitudes. The spectral difference
682 between the two models is also very similar, but again slightly weaker. These
683 differences most likely reflect the issue we previously identified with CSES (and
684 attributed to systematic boom deformation along the orbits), which our improved
685 modelling strategy slightly better mitigates.

686 Figure 10 illustrates the same differences, but for the more relevant backward
687 extrapolation to epoch November 20, 2017, reflecting the errors likely affecting the
688 CGGM candidate model for epoch January 1, 2020. As expected, errors in the radial
689 component are still mainly zonal, but peaking at 37 nT. Spectral differences are the
690 largest for the three first degrees. They reach 20 nT² at degree 1, 50 nT² at degree 2, 30
691 nT² at degree 3 while remaining below 10 nT² at all higher degrees, except for degree 9,
692 which reaches 20 nT². These differences are quite comparable (though more on the high
693 side) to differences observed between the various IGRF 2015 candidate models that
694 were submitted in 2015 (at a similar stage of IGRF model preparation), as can be
695 checked by comparing Figure 10 with Figure 7 of [Thébault et al., \(2015b\)](#).

696 These encouraging comparisons led us to conclude that despite the limitations of the
697 current quality of CSES vector data (limited by the boom deformation issue), and CSES
698 scalar data at high latitude data (see corresponding residual statistics in Table 1), the
699 CGGM candidate model could indeed be proposed as an IGRF 2020 candidate model.

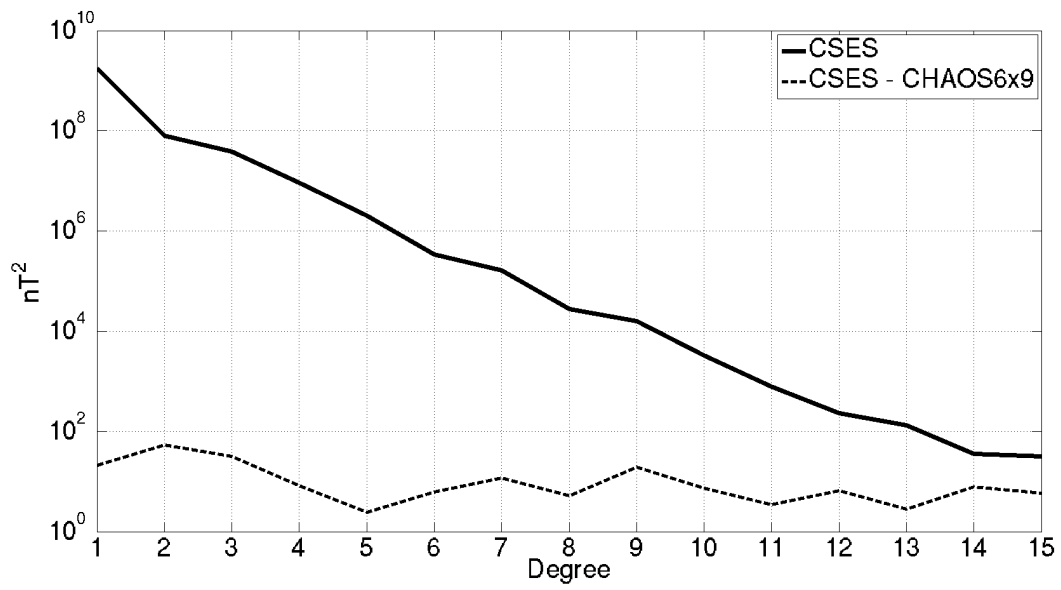


700

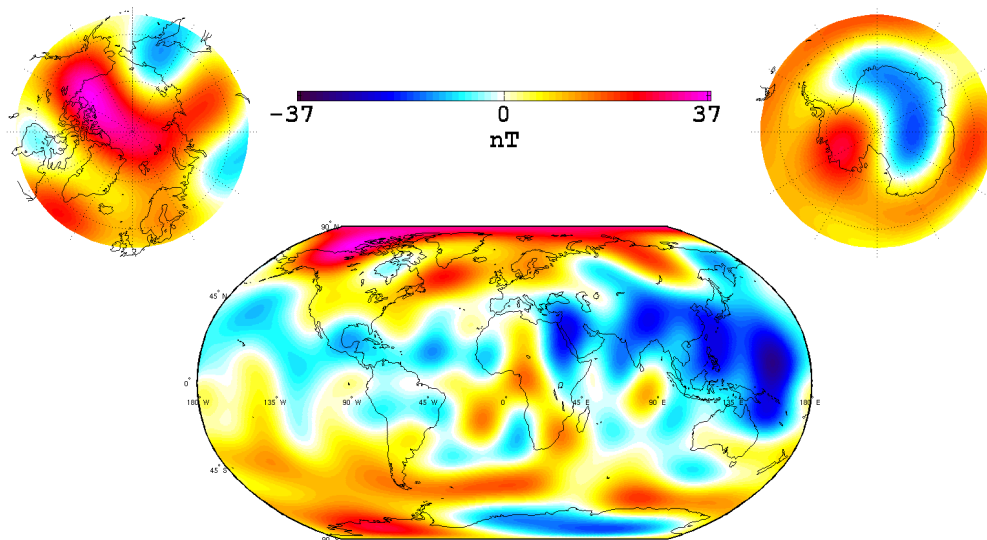


701

702 **Figure 9: CGGM parent model and CHAOS-6-x9 model comparison for epoch**
 703 **December 11, 2018. Top: Lowes-Mauersberger spatial power spectra of the CGGM**
 704 **parent model (solid line) and of the difference between the CGGM parent and**
 705 **CHAOS-6-x9 models (dashed); Bottom: Radial component of the difference between the**
 706 **predictions of the CGGM parent and CHAOS-6-x9 models; All plots at Earth's surface.**



707



708

709 *Figure 10: CGGM parent model and CHAOS-6-x9 model comparison for epoch*

710 *November 20, 2017. Same plotting convention as in Figure 9 (except for colour scale).*

711

712 **Computation of uncertainties for each Gauss coefficient**

713 Realistic uncertainties affecting the Gauss coefficients of the CGGM candidate
714 model were informally requested in addition to the coefficients of the model for
715 submission to the IGRF call. These uncertainties were computed by again assuming that
716 the observed disagreements between the CSES parent model backward extrapolated to
717 epoch November 20, 2017 and the CHAOS6-x9 model computed at the same epoch, are
718 representative of the uncertainties affecting the coefficients of the CGGM candidate
719 model. For each degree n , we computed the following root mean square quantity:

720

$$721 \quad \sigma_n = \sqrt{(2n + 1)^{-1} \sum_{m=0}^n ((dg_n^m)^2 + (dh_n^m)^2)} \quad (1)$$

722

723 where dg_n^m and dh_n^m are the differences in the g_n^m and h_n^m Gauss coefficients
724 between the two models. We then simply assigned this σ_n as our best estimate of the
725 errors (one sigma type) affecting each Gauss coefficient of degree n .

726 This quantity should only be considered as a rough indicator. In particular, it likely
727 underestimates uncertainties affecting zonal coefficients (i.e. g_n^0 Gauss coefficients),
728 by probably a factor 2 (at least for degrees 1 to 3, recall Figure 10; see also [Loves and](#)
729 [Olsen, 2004](#)).

730 **A posteriori quality assessment and conclusion**

731 All candidate models provided in response to the IGRF-13 call having been made
732 available after the October 1, 2019 deadline, and the final IGRF-13 series of models
733 having since been released, we finally looked into the way the CGGM candidate model
734 compares with these models. Eleven IGRF 2020 candidate models were submitted, in
735 addition to the CGGM candidate model, and all twelve models have been used to
736 produce the final IGRF 2020 model, which thus is a model combining all candidate
737 models ([Alken et al., 2020b](#)). The detailed way this was done can be found in [Alken et](#)
738 [al. \(2020a\)](#), and the way each candidate model was prepared can be found in a series of
739 papers to also be found in the present issue. We here refer to these models as the BGS

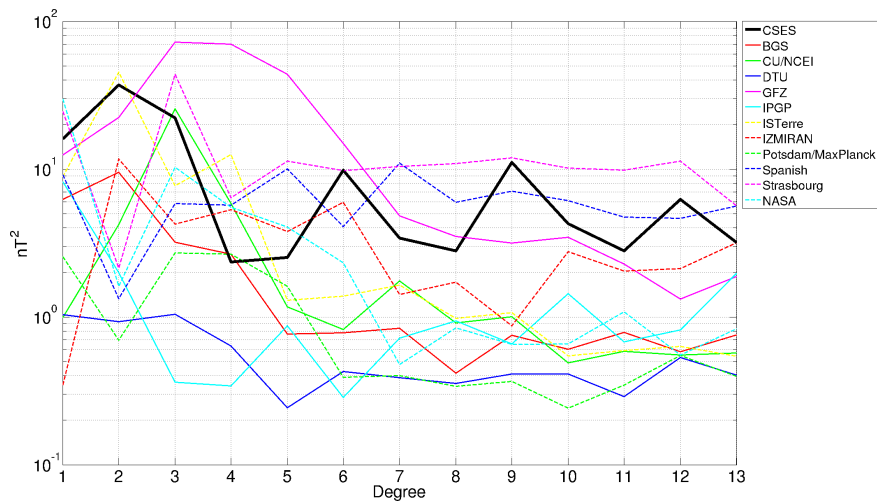
740 model (Brown et al., 2020), the CU/NCEI model (Alken et al., 2020c), the DTU model
741 (Finlay et al., 2020), the GFZ model (Rother et al., 2020), the IPGP model (Ropp et al.,
742 2020), the ISTERre model (Huder et al., 2020), the IZMIRAN model (Petrov and Bondar,
743 2020), the Postdam/MaxPlanck model (Baerenzung et al., 2020), the Spanish model
744 (Pavón Carrasco et al., 2020), the Strasbourg model (Wardinski et al., 2020) and the
745 NASA model (Sabaka et al., 2020).

746 A Lowes-Mauersberger spatial power spectrum of the difference between the CGGM
747 candidate IGRF 2020 model and the now released official IGRF 2020 model, as well as
748 analogous spectra for all other candidate models, are shown in Figure 11 (top), together
749 with a map of the radial component of the difference between the predictions of the
750 CGGM candidate and official IGRF 2020 models (bottom). Comparing this map with
751 those shown in Figures 9 and 10 reveals that these differences are much closer to the
752 differences found when comparing the CGGM parent model to the CHAOS-6-x9 model
753 at central epoch December 11, 2018 (Figure 9) than to those found when carrying the
754 same comparison for the backward extrapolation to epoch November 20, 2017 (Figure
755 10). This shows that the CGGM candidate model does much better than anticipated,
756 despite all the issues identified in the CSES data. The same conclusion holds when
757 comparing Lowes-Mauersberger spectra. In particular, we note that the spectral
758 comparison of the CGGM candidate model with the official IGRF 2020 model always
759 lies within the envelope of the analogous spectral comparison for all the other IGRF
760 2020 candidate models.

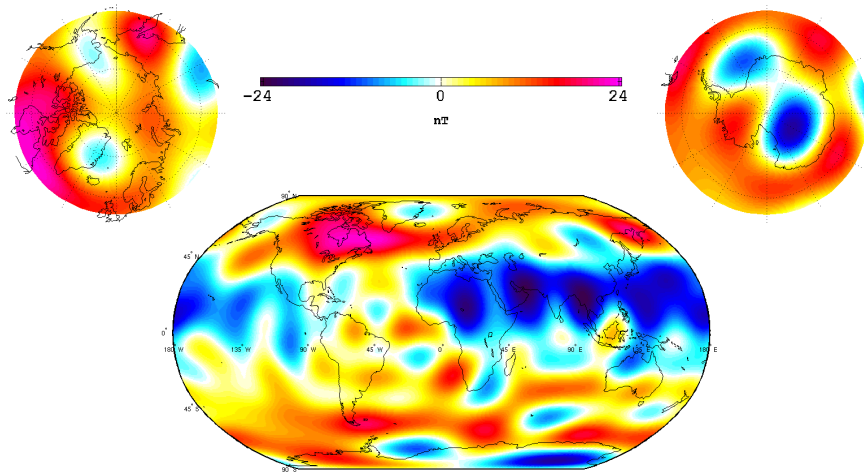
761 The encouraging ability of the CGGM candidate to perform better than anticipated
762 finally led us to also test how well the secular variation associated with the CGGM
763 parent model (referred to as the CGGM SV model in what follows) would have
764 performed, had it been submitted as an IGRF-13 2020-2025 predictive SV candidate
765 model. To test this, similar a posteriori comparisons were performed with the final
766 IGRF-13 2020-2025 predictive SV model, and with the various IGRF-13 2020-2025
767 predictive SV candidate models that were used to build it, and which were produced by

768 either the same teams as the IGRF 2020 candidate models (BGS, CU/NCEI, DTU, GFZ,
769 ISTERre, IZMIRAN, NASA, Potsdam/MaxPlanck, Spanish and Strasbourg models), by
770 other teams led by the same institutions (IPGP model, [Fournier et al., 2020](#)) or by teams
771 led by other institutions. These we refer to as the Japan model ([Minami et al., 2020](#)), the
772 Leeds model ([Metman et al., 2020](#)) and the Max Planck model ([Sanchez et al., 2020](#)). A
773 Lowes-Mauersberger spectral representation of how the CGGM SV model, and all these
774 candidate models, compare to the official IGRF-13 2020-2025 predictive SV model is
775 shown in Figure 12 (top), together with a map of the radial component of the difference
776 between the predictions of the CGGM SV and IGRF-13 2020-2025 predictive SV
777 models (bottom). This comparison reveals that the agreement between the CGGM SV
778 and IGRF-13 2020-2025 predictive SV models is now even better, and that the CGGM
779 SV performs among the best when compared to the fourteen submitted 2020-2025
780 predictive SV candidate models. This is all the more remarkable that the CGGM model
781 is based on a CSES data set completely independent from those used by all other
782 candidate models (which all rely on Swarm data, sometimes also on other data, from e.g.
783 observatories), and that these CSES data still suffer from a number of issues (lack of
784 boom rigidity for the Type 1 vector data, low quality of the high latitude Type 2 scalar
785 data).

786

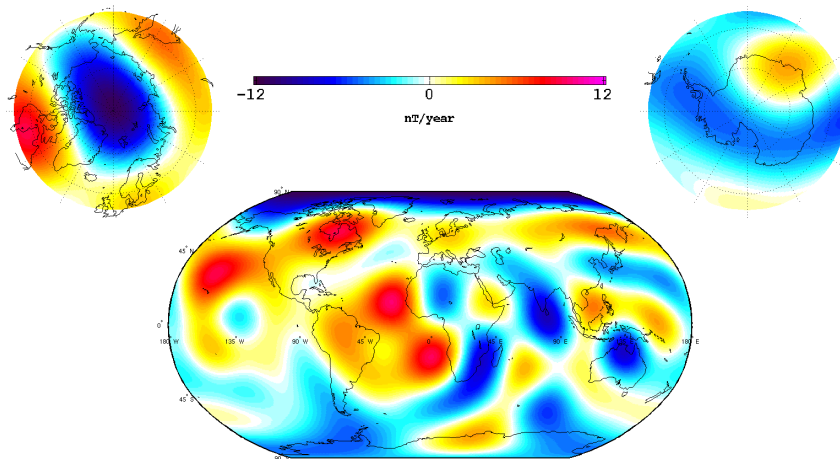
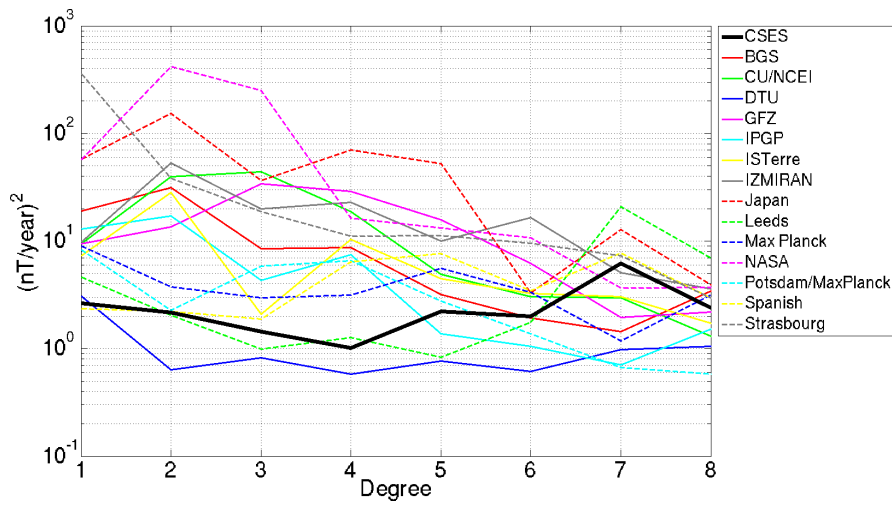


787



788 **Figure 11: CGGM candidate IGRF 2020 model a posteriori assessment.** Top:
 789 Lowes-Mauersberger spectrum of the difference between the CGGM candidate IGRF
 790 2020 model and the final IGRF 2020 model (CSES, thick black line); also shown are
 791 analogous spectra computed for the eleven other candidate models (BGS, solid red;
 792 CU/NCEI solid green; DTU, solid dark blue; GFZ, solid purple; IPGP, solid light blue;
 793 ISTERre, dashed yellow; IZMIRAN, dashed red; Potsdam/MaxPlanck, dashed green;
 794 Spanish, dashed dark blue; Strasbourg, dashed purple; NASA dashed light blue);
 795 Bottom: Radial component of the difference between the predictions of the CGGM
 796 candidate IGRF 2020 and final IGRF 2020 models; All plots at Earth's surface. Gauss
 797 coefficients are used at the officially required $0.01nT$ resolution (closest rounding) for
 798 candidate models and official $0.1nT$ resolution for the final IGRF 2020 model (as
 799 published in [Alken et al., 2020b](#)).

800



801

802 **Figure 12: Comparing the CGGM SV and final IGRF-13 2020-2025 predictive SV**
 803 **models.** Top: Lowes-Mauersberger spectrum of the difference between the CGGM SV
 804 **and the final IGRF-13 predictive SV models (CSES, thick black line); also shown are**
 805 **analogous spectra computed for the fourteen candidate SV models (BGS, solid red;**
 806 **CU/NCEI solid green; DTU, solid dark blue; GFZ, solid purple; IPGP, solid light blue;**
 807 **ISTerre, solid yellow; IZMIRAN, solid grey; Japan, red dashed; Leeds, dashed green;**
 808 **Max Planck, dashed dark blue; NASA, dashed purple; Potsdam/MaxPlanck, dashed**
 809 **light blue; Spanish, dashed yellow; Strasbourg, dashed grey); Bottom: Radial**
 810 **component of the difference between the predictions of the CGGM SV model and the**
 811 **final IGRF-13 2020-2025 predictive SV model; All plots at Earth’s surface. Gauss**
 812 **coefficients are used at the officially required 0.01nT/yr resolution (closest rounding)**
 813 **for candidate models, and official resolution of 0.1nT/yr for the final IGRF-13**
 814 **predictive SV model (as published in Alken et al., 2020b).**

815 The above a posteriori comparisons finally lead us to two very encouraging
816 conclusions. One is that in principle, and despite their current limitations, CSES
817 magnetic data can already be used to produce useful IGRF 2020 and 2020-2025 secular
818 variation candidate models to contribute to the official IGRF-13 2020 and predictive
819 secular variation models for the coming 2020-2025 time period.

820 The other is that now that the main issues affecting the CSES magnetic data have
821 been identified, further improving the quality of its HPM data and making Type 2 scalar
822 data systematically available would undoubtedly be worth the effort. This is quite a
823 challenge. In particular, it would require developing an appropriate description of the
824 way the boom deforms along the orbit of the satellite. But the systematic nature of this
825 deformation, most likely due to the fixed LT of the orbits of CSES (thus always
826 exposed to the Sun in the same way along the orbits), could be taken advantage of. As
827 suggested by the present study, such improved data could then very usefully contribute
828 to the long-term monitoring of the main field and possibly other magnetic field sources,
829 in complement to the data provided by missions such as the ESA Swarm mission.

830

831 **Declarations**

832 **Ethics approval and consent to participate**

833 Not applicable

834 **Consent for publication**

835 Not applicable

836 **List of abbreviations**

837 **BGS:** British Geological Survey

838 **CDSM:** Coupled dark state magnetometer

839 **CGGM:** CSES Global Geomagnetic Field Model

840 **CSES:** China Seismo-Electromagnetic Satellite

841 **CU/NCEI:** University of Colorado/National Centers for Environmental
842 Information

843 **DTU:** Technical University of Denmark

844 **EFD:** Electric Field Detector

845 **ESA:** European Space Agency

846 **FGM:** Fluxgate magnetometer

847 **GFZ:** German Research Centre for Geosciences, Potsdam

848 **GNSS-RO:** GNSS Occultation Receiver

849 **GSM:** Geocentric Solar Magnetospheric

850 **HEPD:** High Energetic Particle Detector

851 **HEPP:** High Energetic Particle Package

852 **HPM:** High precision magnetometer

853 **ICRF:** Inertial Celestial Reference Frame

854 **IAGA:** International Association of Geomagnetism and Aeronomy

855 **IGRF:** International Geomagnetic Reference Field

856 **IPGP:** Institut de Physique du Globe de Paris

857 **ISterre:** Institut des Sciences de la Terre

858 **IzMIRAN:** Pushkov Institute of Terrestrial Magnetism, Ionosphere and

859 Radio Wave Propagation
860 **LAP:** Langmuir Probe
861 **LT:** Local Time
862 **MT:** Magnetotorquer
863 **NASA:** National Aeronautics and Space Administration
864 **NEC:** North-East-Center
865 **QD:** Quasi-dipole
866 **PAP:** Plasma Analyzer
867 **SCM:** Search-Coil Magnetometer
868 **SH:** Spherical harmonic
869 **SM:** Solar Magnetic
870 **STR:** Star imagers
871 **SV:** Secular variation
872 **TBB:** Tri Band Beacon
873 **VFM:** Vector Fluxgate magnetometer on Swarm

874 **Availability of data and materials**

875 CSES HPM data were obtained and are accessible from www.leos.ac.cn.
876 Swarm data and Kp index values were downloaded from the FTP server
877 <ftp://swarm-diss.eo.esa.int>. RC data were taken from
878 <http://www.spacecenter.dk/files/magnetic-models/RC/current/>. The
879 merging electric field Em was computed from Omni data downloaded
880 from ftp://spdf.gsfc.nasa.gov/pub/data/omni/high_res_omni/.

881 **Competing interests**

882 The authors declare that they have no competing interest.

883 **Funding**

884 This work was supported by the National Key R&D Program of China
885 (Grant No. 2018YFC1503500), National Natural Science Foundation of
886 China (Grant No. 41904134), APSCO Earthquake Research Project

887 Phase II and ISSI-BJ project: the electromagnetic data validation and
888 scientific application research based on CSES satellite. GH and PV
889 acknowledge travel support from the European Space Agency through
890 Swarm DISC funding, and support for computation from CNES through
891 the “Suivi et exploitation de la mission Swarm” project.

892 **Authors' contributions**

893 YYY prepared all HPM data, carried out initial model computations with
894 PV, participated in all steps of the study and contributed to the
895 manuscript; GH designed the study, wrote the manuscript, and
896 participated in all steps of the study; PV carried out all model
897 computations discussed in the manuscript and participated in all steps of
898 the study; XHS, the chief scientist of CSES, coordinated the cooperation
899 of the research group and followed the entire study; ZMZ coordinated
900 the needed HPM level 0 data from CRESDA and followed the entire
901 study. BZ and WM led the design of the HPM instruments and its main
902 processing chain; NO and LTC contributed to the initial data quality
903 analysis and assisted in the modelling strategy choices; JPH and FG led
904 the production of HPM data, with the help of JBY and JW; XMZ and
905 LWW contributed to the development of CSES application center and
906 determination of HPM level 2 products; SGY, JPD and XHZ designed
907 the satellite platform and helped in the analysis of star imager data; BJC
908 carried out the performance verification of the HPM; AP and RL had the
909 lead for the CDSM instrument development and carried out the
910 performance verification of the CDSM data pre- and post-launch; JL
911 contributed to the analysis of HPM Level 0 data; YYW and XDZ
912 contributed to the data analysis. All authors read and approved the final
913 manuscript.

914 **Acknowledgements**

915 This work made use of the data from CSES mission, a project funded by
916 the China National Space Administration (CNSA) and the China
917 Earthquake Administration (CEA). The authors thank Ciaran Beggan and
918 an anonymous reviewer for their very useful comments that helped
919 improve this manuscript.
920

921 **References**

- 922 Alken P, Thébault E, Beggan C, Aubert J, Baerenzung J, Brown W, Califf S, Chulliat A,
923 Cox G, Finlay CC, Fournier A, Gillet N, Hammer MD, Holschneider M, Hulot G,
924 Korte M, Lesur V, Livermore P, Lowes F, Macmillan S, Nair M, Olsen N, Ropp G,
925 Rother M, Schnepf NR, Stolle C, Toh H, Vervelidou F, Vigneron P, Wardinski I
926 (2020a) Evaluation of candidate models for the 13th International Geomagnetic
927 Reference Field. *Earth Planets Space*, submitted.
- 928 Alken P, Thébault E, Beggan CD, Amit H, Aubert J, Baerenzung J, Bondar TN, Brown
929 W, Califf S, Chambodut A, Chulliat A, Cox G, Finlay CC, Fournier A, Gillet N,
930 Grayver A, Hammer MD, Holschneider M, Huder L, Hulot G, Jager T, Kloss C, Korte
931 M, Kuang W, Kuvshinov A, Langlais B, Léger JM, Lesur V, Livermore PW, Lowes
932 FJ, Macmillan S, Mound JE, Nair M, Nakano S, Olsen N, Pavón-Carrasco FJ, Petrov
933 VG, Ropp G, Rother M, Sabaka TJ, Sanchez S, Saturnino D, Schnepf NR, Shen X,
934 Stolle C, Tangborn A, Tøffner-Clausen L, Toh H, Torta JM, Varner J, Vervelidou F,
935 Vigneron P, Wardinski I, Wicht J, Woods A, Yang Y, Zeren Z, Zhou B (2020b)
936 International Geomagnetic Reference Field: the thirteenth generation. *Earth, Planets
937 and Space*, accepted..
- 938 Alken P, Chulliat A, Nair M (2020c) University of Colorado / National Centers for
939 Environmental Information IGRF-13 candidate models. *Earth, Planets and Space*, in
940 preparation.
- 941 Backus G (1970) Non-uniqueness of the external geomagnetic field determined by
942 surface intensity measurements. *J Geophys Res* 75:6339-6341.
943 doi:10.1029/JA075i031p06339.
- 944 Baerenzung J, Holschneider M, Wicht J, Lesur V, Sanchez S (2020) The Kalmag model
945 as a candidate for IGRF-13. *Earth, Planets and Space*, submitted
- 946 Bartels J (1949) The standardized index, Ks, and the planetary index Kp. *IATME Bull*
947 12b, IUGG Publ Office, Paris: 97–112
- 948 Brown W, Beggan CD, Cox G, Macmillan S (2020) The BGS candidate models for

949 IGRF-13 with a retrospective analysis of IGRF-12 secular variation forecasts. *Earth,*
950 *Planets and Space*, submitted.

951 Cheng BJ, Zhou B, Magnes W, Lammegger R, Pollinger A (2018) High precision
952 magnetometer for geomagnetic exploration onboard of the China
953 Seismo-Electromagnetic Satellite. *Sci China Tech Sci* 61 (5): 659–668.
954 doi:10.1007/s11431-018-9247-6.

955 Farquharson CG, Oldenburg DW (1998) Non-linear inversion using general measures of
956 data misfit and model structure. *Geophys J Int* 134(1):213-227. doi:
957 10.1046/j.1365-246x.1998.00555.x

958 Finlay CC, Olsen N, Kotsiaros S, Gillet N, Tøffner-Clausen L (2016) Recent
959 geomagnetic secular variation from Swarm and ground observatories as estimated in
960 the CHAOS-6 geomagnetic field model. *Earth Planets Space* 68:112. doi:
961 10.1186/s40623-016-0486-1.

962 Finlay CC, Kloss C, Olsen N, Hammer M, Tøffner-Clausen L, Grayver A, Kuvshinov A
963 (2020) The CHAOS-7 geomagnetic field model and observed changes in the South
964 Atlantic Anomaly. *Earth, Planets and Space*, submitted.

965 Fournier A, Aubert J, Lesur V, Ropp G (2020) A secular variation candidate model for
966 IGRF-13 based on Swarm data and ensemble inverse geodynamo modelling. *Earth*
967 *Planets Space*, accepted.

968 Holme R, Bloxham J (1996) The treatment of attitude errors in satellite geomagnetic data.
969 *Phys Earth Planet Int* 98:221-233. doi: 10.1016/S0031- 9201(96)03189-5.

970 Huder L, Gillet N, Finlay CC, Hammer MD, Tchoungui H (2020) COV-OBS.x2: 180 yr
971 of geomagnetic field evolution from ground-based and satellite observations. *Earth,*
972 *Planets and Space*, accepted.

973 Hulot G, Vigneron P, Léger J-M, Fratter I, Olsen N, Jager T, Bertrand F, Brocco L, Sirol
974 O, Lalanne X, Boness A, Cattin V (2015a) Swarm’s absolute magnetometer
975 experimental vector mode, an innovative capability for space magnetometry. *Geophys*
976 *Res Lett* 42:1352-1359. doi: 10.1002/2014GL062700.

977 Hulot G, Sabaka TJ, Olsen N, Fournier A (2015b) The Present and Future Geomagnetic
978 Field. In: Gerald Schubert (editor-in-chief), *Treatise on Geophysics*, 2nd Edition, Vol.
979 5, pp 33-78, Elsevier, Oxford, doi:10.1016/B978-0-444-53802-4.00096-8.

980 Kan JR, Lee LC (1979) Energy coupling function and solar wind-magnetosphere dynamo.
981 *Geophys Res Lett*, 6:577–580. doi:10.1029/GL006i007p00577.

982 Khokhlov A, Hulot G, Le Mouél JL (1997) On the Backus effect I. *Geophys J Int*
983 130:701-703. doi:10.1111/j.1365-246X.1997.tb01864.x.

984 Khokhlov A, Hulot G, Le Mouél JL (1999) On the Backus effect II. *Geophys J Int*
985 137:816-820. doi:10.1046/j.1365-246x.1999.00843.x.

986 Lowes FJ (1966) Mean-square values on sphere of spherical harmonic vector fields. *J*
987 *Geophys Res* 71:2179. doi:10.1029/JZ071i008p02179.

988 Lowes FJ (1975) Vector errors in spherical harmonic analysis of scalar data. *Geophys J R*
989 *Astr Soc* 42(2): 637-651. doi:

990 Lowes FJ, Olsen N (2004) A more realistic estimate of the variances and systematic
991 errors in spherical harmonic geomagnetic field models. *Geophys J Int* 157:1027-1044.
992 doi:10.1111/j.1365-246X.2004.02256.x

993 Macmillan S, Finlay C (2011) The international geomagnetic reference field. In : Mande
994 M, Korte M (eds) *Geomagnetic Observations and Models*, vol 5, IAGA Special
995 Sopron Book Series, Springer, Heidelberg, pp 265-76

996 Mauersberger P (1956) Das Mittel der Energiedichte des geomagnetischen Hauptfeldes
997 an der Erdoberfläche und seine säkulare Änderung. *Gerl Beitr Geophys* 65:207–15

998 Maus S, Luehr H (2005) Signature of the quiet-time magnetospheric magnetic field and
999 its electromagnetic induction in the rotating Earth. *Geophys J Int* 162(3): 755-763. doi:
1000 10.1111/j.1365-246X.2005.02691.x

1001 Menvielle M, Berthelier A (1991) The K-derived planetary indices: description and
1002 availability. *Reviews of Geophysics*, 29(3):415-432. doi:10.1029/91RG00994.

1003 Metman MC, Beggan CD, Livermore PW, Mound JE (2020) Forecasting yearly
1004 geomagnetic variation through sequential estimation of core flow and magnetic

1005 diffusion. *Earth, Planets and Space*, accepted

1006 Minami T, Nakano S, Lesur V, Takahashi F, Matsushima M, Shimizu H, Nakashima R,
1007 Taniguchi H, Toh H (2020) A candidate secular variation model for IGRF-13 based on
1008 MHD dynamo simulation and 4DEnVar data assimilation, *Earth Planets Space*,
1009 accepted.

1010 Olsen N, Hulot G, Lesur V, Finlay CC, Beggan CC, Chulliat A, Sabaka TJ,
1011 Floborghagen R, Friis-Christensen E, Haagmans R, Kotsiaros S, Lühr H,
1012 Tøffner-Clausen L, Vigneron P (2015) The Swarm Initial Field Model for the 2014
1013 geomagnetic field. *Geophys Res Lett* 42:1092-1098. doi: 10.1002/2014GL062659.

1014 Olsen N, Lühr H, Finlay CC, Sabaka TJ, Michaelis I, Rauberg J, Tøffner-Clausen L
1015 (2014) The CHAOS-4 geomagnetic field model. *Geophys J Int* 197:815–27. doi:
1016 10.1093/gji/ggu033.

1017 Pavón-Carrasco FJ, Marsal S, Torta JM, Catalan M, Martin-Hernandez F, Tordesillas JM
1018 (2020) Bootstrapping Swarm and observatory data to generate candidates for the
1019 DGRF and IGRF-13. *Earth, Planets and Space*, accepted.

1020 Petrov VG, Bondar TN (2020) IZMIRAN sub-model for IGRF-13. *Earth, Planets and*
1021 *Space*, in preparation.

1022 Pollinger A., Lammegger R, Magnes W, Hagen C, Ellmeier M, Jernej I, Leichtfried M,
1023 Kürbisch C, Maierhofer R, Wallner R, Fremuth G, Amtmann C, Betzler A, Delva M,
1024 Prattes G and Baumjohann W (2018) Coupled dark state magnetometer for the China
1025 seismo-electromagnetic satellite. *Measurement Sci Tech* 29(9).
1026 doi:10.1088/1361-6501/aacde4

1027 Pollinger A., Amtmann C, Betzler A, Cheng B, Ellmeier M, Hagen C, Jernej I,
1028 Lammegger R, Zhou B, Magnes W (2020) In-orbit results of the Coupled Dark State
1029 Magnetometer aboard the China Seismo-Electromagnetic Satellite. *Geosci Instrum*
1030 *Method Data Syst*, 9:275-291, doi:10.5194/gi-9-275-2020.

1031 Richmond AD (1995) Ionospheric electrodynamics using magnetic Apex coordinates. *J*
1032 *Geomagn Geoelectr* 47:191–212. doi:10.5636/jgg.47.191.

1033 Ropp G, Lesur V, Baerenzung J, Holschneider M, Sequential modelling of the Earth's
1034 core magnetic field. *Earth Planets Space*, accepted.

1035 Rother M, Korte M, Morschhauser A, Vervelidou F, Matzka J, Stolle C (2020) The
1036 Mag.num core field model as a parent for IGRF-13, and the recent evolution of the
1037 South Atlantic Anomaly. *Earth, Planets and Space*, submitted.

1038 Sabaka TJ, Tøffner-Clausen L, Olsen N, Finlay CC (2020) CM6: A Comprehensive
1039 Geomagnetic Field Model Derived From Both CHAMP and Swarm Satellite
1040 Observations. *Earth, Planets and Space*, accepted

1041 Sanchez S, Wicht J, Baerenzung J (2020) Predictions of the geomagnetic secular
1042 variation based on the ensemble sequential assimilation of geomagnetic field models
1043 by dynamo simulations. *Earth, Planets and Space*, submitted.

1044 Shen XH, Zhang XM, Yuan SG, Wang LW, Cao JB, Huang JP, Zhu XH, Piergiorgio P,
1045 Dai JP (2018) The state-of-the-art of the China Seismo-Electromagnetic Satellite
1046 mission. *Sci China Tech Sci* 61(5): 634–642. doi:10.1007/s11431-018-9242-0

1047 Thébaud E, Finlay CC, Beggan CD, Alken P, Aubert J, Barrois O, Bertrand F, Bondar T,
1048 Boness A, Brocco L, Canet E, Chambodut A, Chulliat A, Coïsson P, Civet F, Du A,
1049 Fournier A, Fratter I, Gillet N, Hamilton B, Hamoudi M, Hulot G, Jager T, Korte M,
1050 Kuang W, Lalanne X, Langlais B, Léger JM, Lesur V, Lowes FJ, Macmillan S,
1051 Manda M, Manoj C, Maus S, Olsen N, Petrov V, Ridley V, Rother M, Sabaka TJ,
1052 Saturnino D, Schachtschneider R, Sirol O, Tangborn A, Thomson A, Tøffner-Clausen
1053 L, Vigneron P, Wardinski I, Zvereva T (2015a) International Geomagnetic Reference
1054 Field: the 12th generation. *Earth Planets Space* 67:79.
1055 doi:10.1186/s40623-015-0228-9.

1056 Thébaud E, Finlay CC, Alken P, Beggan CD, Canet E, Chulliat, A, Langlais B, Lesur V,
1057 Lowes FJ, Manoj C, Rother M, Schachtschneider R (2015b) Evaluation of candidate
1058 geomagnetic field models for IGRF-12. *Earth Planets Space* 67:112. doi:
1059 10.1186/s40623-015-0273-4.

1060 Vigneron P, Hulot G, Olsen N, Léger JM, Jager T, Brocco L, Sirol O, Coïsson P, Lalanne

1061 X, Chulliat A, Bertrand F, Boness A, Fratter I (2015) A 2015 International
1062 Geomagnetic Reference Field (IGRF) Candidate model based on Swarm's
1063 experimental absolute magnetometer vector mode data. *Earth Planets Space* 67:95.
1064 doi:10.1186/s40623-015-0265-4.

1065 Wardinski I, Saturnino D, Amit H, Chambodut A, Langlais B, Manda M, Thébaud E
1066 (2020) Geomagnetic core field models and secular variation forecasts for the 13th
1067 International Geomagnetic Reference Field (IGRF-13). *Earth, Planets and Space*,
1068 submitted.

1069 Yang YY, Zeren ZM, Shen XH, Chu W, Huang JP, Wang Q, Yan R, Xu S, Lu HX, Liu
1070 DP (2020a) The first intense geomagnetic storm event recorded by the China
1071 Seismo-Electromagnetic Satellite. *Space Weather* 18 e2019SW002243.
1072 doi:10.1029/2019SW002243.

1073 Yang YY, Zhou B, Hulot G, Olsen N, Xiong C, Stolle C, Shen XH, Zeren ZM., Huang
1074 JP, Zhu XH., Pollinger A (2020b) CSES high precision magnetometer data products
1075 and some initial results from an intense geomagnetic storm. To be submitted.

1076 Zhou B, Yang YY, Zhang YT, Gou XC, Cheng BJ, Wang JD, Li L (2018) Magnetic field
1077 data processing methods of the China Seismo-Electromagnetic Satellite. *Earth Planet*
1078 *Phys* 2(6): 455–461. doi:10.26464/epp2018043.

1079 Zhou B, Cheng B, Gou X, et al (2019) First in-orbit results of the vector magnetic field
1080 measurement of the High Precision Magnetometer onboard the China
1081 Seismo-Electromagnetic Satellite. *Earth Planet Space* 71: 119.
1082 doi:10.1186/s40623-019-1098-3.